2021-10-28

CHOS gas/fluidinduced reduction in ureilites

Langendam, AD

10.1111/maps.13755
Meteoritics and Planetary Science
Wiley

CHOS gas/fluid-induced reduction in ureilites

Andrew D. Langendam[1], Andrew G. Tomkins[1]*, Katy A. Evans[2], Nicholas C. Wilson[3], Colin M. MacRae[3], and Natasha R. Stephen[4], Aaron Torpy[3]

[1]School of Earth, Atmosphere and Environment, Monash University, Melbourne, Victoria 3800, Australia.

[2]Department of Applied Geology, Curtin University, Perth, WA 6845, Australia

[3]CSIRO Mineral Resources, Microbeam Laboratory, Victoria 3169, Australia

[4]Plymouth Electron Microscopy Centre, University of Plymouth, Drake Circus, Plymouth, Devon, PL4 8AA, United Kingdom

*Corresponding Author Details:

Email: Andy.Tomkins@monash.edu

Phone: +61 3 9905 1643

ABSTRACT

Ureilite meteorites contain regions of localized olivine reduction to Fe metal widely accepted to have formed by redox reactions involving oxidation of graphite; a process known as secondary smelting. However, the possibility that other reductants might be responsible for this process has largely been ignored. Here, seventeen ureilite samples are investigated to assess whether, instead of smelting involving only solid reactants, a CHOS gas/fluid could have caused much of the smelting. Features consistent with gas- or supercritical fluid-driven reduction were found to be abundant in all ureilites, such as fracture-focused smelting, plume-like reaction fronts and addition of sulfur. Many of these are developed away from graphite. In some ureilites, it is clear that the redox process coincided with annealing, and we suggest that this was caused by enhanced diffusion facilitated by a higher density gas or fluid, rather than slow cooling, which requires elevated pressure. The C-CO and CH_4-C-H_2O buffers were modelled to examine their relative potential to drive reduction. This modelling showed that a CH_4-rich fluid is able to produce the observed mineral compositions at elevated pressures. This result, coupled with the observed textures, is used to develop a likely series of reactions. We suggest that at higher pressures a H_2-CH_4-H_2S-S_2-bearing fluid-like phase, and at lower pressures an equivalent gas, was able to infiltrate grain boundaries and fine fractures. Sulfidation to form troilite may have acted to maintain highly reduced gas/fluid conditions. The presence of hydrocarbons in ureilites supports a role for reduction driven by CHOS gas/fluid.

INTRODUCTION

Ureilites are carbon-rich primitive achondrite meteorites consisting primarily of olivine, pigeonite, and in some samples, orthopyroxene and/or augite (Berkley et al., 1980; Mittlefehldt et al., 1998; Warren and Huber, 2006; Zolensky et al., 2010; Goodrich et al., 2015). Most ureilites are the residues of ~15-22% fractional melt extraction from a chondritic protolith in the mantle of the ureilite parent body (UPB), which reached up to 1280°C (cf. Singletary and Grove, 2003; Goodrich et al., 2007; Warren, 2011; Collinet and Grove, 2020).

Unlike all other achondrites, ureilites have distinct $\Delta^{17}O$ heterogeneity (e.g., Franchi et al., 2001). On this basis, it has been suggested that ureilites formed from a carbonaceous chondrite precursor (Rubin, 1988; Kita et al., 2004). However, the heavy stable isotope signature of ureilites is distinct from the carbonaceous chondrites and is consistent with an asteroid that likely formed in the inner solar system (e.g., Scott et al., 2018). Based on the large variations in oxygen and carbon isotopes, and their correlation with olivine FeO and Fe/Mn, it has been suggested that the UPB accreted from two isotopically and geochemically distinct parent bodies (Barrat et al., 2017). A similar mixing model suggests that prior to silicate melting, FeNi metal was variably oxidised to FeO through reaction with heterogeneous amounts of H_2O, which had different $\Delta^{17}O$ to the silicates (Sanders et al., 2017). Recent work investigating the noble gas variations in ureilites as a function of $\Delta^{17}O$ and $\delta^{13}C$ also suggested that the two-component mixing model is likely (Broadley et al., 2020).

The unique texture that distinguishes ureilites from other achondrites consists of primary olivine crystals (Fo_{74-97}; Goodrich et al., 2015) with extremely FeO-depleted rims (commonly ~Fo_{99}) containing numerous small metallic Fe particles adjacent to graphite–diamond mixtures,

which form grain boundary networks (Warren and Rubin, 2010). These reduced rims indicate that a secondary redox process was active at high temperatures after melt extraction had taken place (Berkley et al., 1980; Walker and Grove, 1993). The current explanation for this texture is a solid-state redox reaction between olivine and graphite, producing CO gas through the following reactions (Warren and Huber, 2006):

$$C^0 + FeMgSiO_4 = MgSiO_3 + Fe^0 + CO \quad [1]$$

$$2C^0 + 2FeMgSiO_4 = Mg_2SiO_4 + SiO_2 + 2Fe^0 + 2CO \quad [2]$$

This process is commonly referred to as secondary smelting. The production of gas means that these reactions are highly sensitive to pressure changes, proceeding at progressively lower temperatures as pressure drops. Even at very high temperatures, they can only proceed at low pressure; estimates range from ~5-30 bar for FeO-rich ureilites to ~50-140 bar for FeO-poor ureilites (Goodrich et al., 1987; Warren and Kallemeyn, 1992; Walker and Grove, 1993; Sinha et al., 1997; Singletary and Grove, 2003; Collinet and Grove, 2020). To explain how very high temperatures and low pressures led to this late smelting, it has been suggested that an impact disrupted the UPB, leaving hot mantle fragments at lower pressure, thereby promoting smelting (Warren and Huber, 2006). In this model, rapid cooling also allows preservation of the smelting textures (which are not preserved in all ureilites). Given the temperature of the Type 3-4 transition in chondrites (the transition to Fe-Mg diffusion in olivine), this cooling needs to reach temperatures below ~600°C rapidly to preserve the subtle Fe-Mg zoning in olivine seen in some ureilites. The presence of uninverted pigeonite also requires rapid cooling (e.g., Goodrich et al., 2015) in those ureilites that do not preserve subtle olivine zoning to below the

blocking temperature of Ca-Fe-Mg diffusion in pigeonite, which is on the order of 900°C (Tomkins et al., 2020).

In this paper, we investigate an alternative hypothesis to smelting involving solid reactants, whereby a reduced CHOS fluid drove much of the secondary smelting seen in ureilites and proceeded at a variety of pressures controlled by fragment size. This hypothesis is evaluated by examination of ureilite textures, combined with calculations evaluating the effects of decompression on the system, and the pressure-temperature conditions required for methane-driven smelting compared with graphite-driven smelting.

METHODS

Seventeen ureilite samples (Table 1) were examined via optical petrography, scanning electron microscope (SEM) and electron probe microanalysis (EPMA) and mapping. Optical microscopy was used to characterize the primary mineral relationships. Regions of interest were mapped using JEOL 8500F and JEOL 8530F-CL HyperProbes at CSIRO Microprobe Laboratory in Melbourne. Wavelength and energy dispersive spectrometry were acquired in parallel with spectral cathodoluminescence (CL) using a grating spectrometer (MacRae et al., 2013). Extraction of elemental maps, CL maps and the extraction of X-ray and CL spectra were performed using inhouse software *Chimage* (Torpy et al., 2020). Microanalysis of silicate glass was performed with a 12 kV accelerating voltage, 15 nA beam current, and spot size was at least 1 μm to minimise migration under the electron beam. Because of the limitations of beam interaction volume, we could only analyse the largest areas of glass, which occur in grain boundary veinlets. Elements analysed were Na, Mg, Al, Si, K, Ca, Fe and Cr, with oxygen

112 calculated by stichometry. A full PRZ matrix correction implemented in *STRATAGem* was
113 performed. Standards used were wollastonite ($CaSiO_3$), magalox ($MgAl_2O_4$), albite
114 ($NaAlSi_3O_8$), adularia ($KAlSi_3O_8$), hematite (Fe_2O_3) and eskolaite (Cr_2O_3). Na, Mg, Al, Si peak
115 counting times were 10 s, and Ca, K, Fe and Cr had peak counting times of 20 s. Detection
116 limits were between 150-300 ppm and measured concentrations were at least an order of
117 magnitude above. Back scattered electron (BSE) images were also obtained. Additional BSE
118 and X-ray element mapping were conducted at Plymouth Electron Microscopy Centre,
119 University of Plymouth, using a JEOL 7001F Scanning Electron Microscope (SEM) equipped
120 with an Oxford Instruments X-Max 80 mm^2 energy dispersive spectroscopy (EDS) detector.
121 SEM-EDS data were acquired and processed using Oxford Instruments AZtec software.
122
123 Chemical equilibrium modelling was conducted to evaluate the relative positions of the C-CO,
124 CH_4-C and olivine-orthopyroxene-iron (OPI) buffers, using the compositions of olivine and
125 pyroxene found in ureilites. This approach is important because fO_2 varies considerably as a
126 function of the fayalite and ferrosilite content of olivine and pyroxene respectively. The
127 positions of the buffers, for fixed values of input compositional variables, where necessary,
128 were calculated using THERMOCALC tc340i with the tcds55S dataset (Holland and Powell, 2011)
129 in mode 0. Mode 0 calculations determine the chemical potentials of the end-members used in
130 the calculations at the pressures and temperatures of interest. These were used to calculate the
131 equilibrium constant of the chosen reactions, and from this, the value of the oxygen activity.
132 So for example, for the general reaction:
133
134 $$n_a\,a + n_b\,b = n_c\,c + n_O\,O_2 \qquad [3]$$
135

where n_a, n_b, n_c and n_O are stoichiometric coefficients for the end-members a, b, c and O_2 respectively, the oxygen activity can be calculated from the expression:

$$\text{Log}\,[O_2] = 1/n_O\,(n_a\,\text{Log}[a] + n_b\,\text{Log}[b] - n_c\,\text{Log}[c] - (\Delta G^\theta/2.303\,R\mathit{T})). \quad [4]$$

Square brackets indicate the activity of the end-member, ΔG^θ is the standard state Gibbs free energy change for the reaction at the pressure and temperature of interest, R is the universal gas constant, and T is the temperature. Oxygen activities are calculated relative to a standard state of the pure gas at 1 bar, so the activity is equal to the fugacity. Activities of the iron end-members of the silicate phases and for the fluid end-members were calculated assuming ideal activity-composition relationships. Mixing in olivine and orthopyroxene is not ideal, but the uncertainties introduced by the assumption are only a fraction of a log unit, so this approach is considered adequate. Activities of iron, wustite and graphite were assumed to be one. Calculations were made for CH_4 activities of 0.8, 0.95 and 0.999, and for the C-CO buffer assuming that the fluid was dominated by CO (i.e., a hydrogen-free system). These curves were then plotted against the olivine-pyroxene-iron buffer using a representative range of fayalite and ferrosilite values for natural ureilites. The calculations were conducted at two pressures, 100 and 1000 bar. The pressure of 100 bar equates to a depth of ~29 km in a 200 km diameter body, the minimum size of the UPB (Goodrich et al., 2007), whereas 1000 bar equates to a depth of 109 km in a 534 km diameter body (see discussion on UPB size below). Methane is a supercritical fluid above about 30 bar.

Calculations were also performed using the software *D-Compress* (Burgisser et al., 2015) to examine the effect of decompression on gas/fluid coexisting with silicate melt. The intention here was to start with a system under modest pressure (P) at high temperature (T) consistent

with the deep mantle of a 534 km UPB (10% is at P > 1000 bar), then decompress to examine: (1) partitioning between melt and gas in a system in equilibrium with excess FeS and C, and (2) the effects of decompression on adiabatic cooling. The starting P and T were 1000 bar and 1280°C at fO_2 of ΔNNO -3 (1 log unit above the Fe-FeO buffer, appropriate for the most oxidised ureilites; Goodrich et al., 2013a) for the adiabatic decompression calculations. Starting T was 1280°C for the gas partitioning calculations, examining several pressures, and changing fH_2O/fCO_2 from 0.25 to 0.001, using the basaltic bulk composition for the silicate melt provided by D-Compress. The results were briefly compared with those for the rhyolitic bulk composition provided. The bulk compositions of silicate glasses in ureilites tend to approximately vary between these end-members (see below).

RESULTS

Petrography

Most of the 17 ureilites examined in this study (with olivine in the range $Fa_{11.4}$-$Fa_{23.8}$) have typical equilibrated metamorphic textures with 120º triple junctions between large olivine and pyroxene crystals (all are hot desert finds; one from the Nullarbor in Australia, and the remainder from northwest Africa; Table 1). Three samples (NWA 4225, NWA 11893, NWA 11900) have a network of large poikiloblastic pyroxene grains with sub-spherical olivine chadacrysts; textures that indicate equilibrium crystallization of the pyroxene from silicate melt. Of these, NWA 11900 is augite-bearing, whereas the other two are not. In addition, NWA 11754 is augite- and chromite-bearing, but does not have these poikiloblastic textures, and is likely an igneous cumulate (Collinet and Grove, 2020). Three ureilites have strong silicate mineral elongation with aspect ratios as high as 15:1 (long axis/short axis; Table 1), six have

186 moderate mineral elongation, and another six have weak to absent mineral elongation, although
187 it is noted that the cutting orientation affects recognition of this texture. These features
188 represent the primary ureilite texture that equilibrated at peak temperature and pressure (e.g.,
189 Goodrich et al., 2015).
190
191 As in numerous previous studies (good overview in Warren and Huber, 2006), we found well-
192 developed smelted regions at graphite-olivine interfaces in all coarse-grained ureilites,
193 recognised by the presence of numerous small metal grains embedded in 50-100 μm wide FeO-
194 depleted domains at the margins of coarse olivine grains (Figs. 1, 2). However, many examples
195 are seen where graphite lacks or has minimal adjacent smelting of olivine, despite widespread
196 smelting in close proximity (Fig. 1D), and smelting also typically occurs well away from
197 graphite/diamond (Table 1), on fractures and along grain boundaries.
198
199 In most samples, olivine smelting ranges from subtle (NWA 7630) to strong (NWA 4225), and
200 in a few ureilites pyroxene grains are also affected. Preferential smelting of pyroxene coupled
201 with strong annealing of olivine, as described by Warren and Rubin (2010), was observed in
202 NWA 11755. We also examined two fine-grained ureilites (NWA 5996 and NWA 7983),
203 which are typically characterized by strongly reduced and highly porous olivine and pyroxene
204 (as indicated by low FeO; e.g., Horstmann and Bischoff, 2014).
205
206 Fracture-associated smelting (Figs. 1, 2; see also Rubin, 2006) is widespread in the coarse-
207 grained ureilites that we examined. This texture has the same mineralogical relationships as
208 grain boundary smelting, although typically lacking graphite/diamond, and the smelted
209 domains around fractures may be narrower. Typically, these fracture-associated domains are
210 connected to smelted grain boundary regions (Figs. 1B, 2A). Some fractures in olivine have

Fe-depleted margins lacking metal or troilite, and contain a linear set of metal and/or troilite grains only within the fracture (Fig. 2A). In some areas, minor fractures with associated Fe depletion propagate from a larger fracture (Fig. 1A). These narrow fractures also contain very small metal particles. Some olivine grains also have parallel sets of smelted fractures (Fig. 1C). In some samples, graphite-associated smelting is strongly subordinate to fracture-associated smelting. In general, the intensity of smelting is hierarchical: the smallest fractures have the narrowest smelted margins, larger fractures have wider margins, and these intersect with complex domains containing the most intense smelting (Figs. 1A-C, 2A).

Smelting is common adjacent to troilite-metal veins, well away from graphite/diamond (Figs. 1D, 2D). In most ureilites, these coarse metal-troilite veins occur along grain boundaries (Goodrich et al., 2013b), commonly enveloped in small amounts of silicate melt (defined by Si-rich glass, fine euhedral pyroxene crystals, quartz; Goodrich, 1992).

Element maps of smelted domains reveal significant heterogeneity in texture and mineral association between samples. Within smelted domains, Fe-depleted olivine is predominant (e.g., NWA 2705), and in others forsterite coexists with fine-grained enstatite (e.g., NWA 3140). Some, particularly NWA 4471, contain numerous small Si-rich silicate melt patches within smelted domains (Fig. 3A), many of which contain a spherical metal-troilite particle indicating an immiscible melt system. Well-rounded voids occur both along grain boundaries and within individual crystals (Fig. 3). There is a clear association between smelting and production of more Si-rich phases (Fig. 3B, E), which can be enstatite, quartz or aluminous silicate glass. Microprobe analyses of the glass in NWA 4471 show a clear trend of SiO_2 addition (Fig. 4). Fine silicate glass veinlets (a few microns width) with Fe-depleted margins transect pyroxenes in several ureilites (Fig. 3C), and these typically contain tiny spherical

metal-troilite melt droplets or metal/troilite veins and voids. Other fine glass-bearing veinlets sit along grain boundaries in many ureilites (Goodrich, 1992; Rosen et al., 2019; Tomkins et al., 2020) and contain euhedral microcrystals of ortho- and clinopyroxene and globular metal/troilite indicating immiscible metal-sulfide melt (Fig. 3D).

Troilite grains occur amongst the small metal particles within smelted margins in both grain boundary and fracture-based smelting in most ureilites (Fig. 2; Table 1). In several ureilites, troilite is more abundant than Fe metal in smelted domains. NWA 3156 is unusual in that it contains highly abundant fine-grained troilite throughout FeO-poor olivine grains, and in this sample there is no smelting-generated fine-grained metal (Fig. 2D).

In some ureilites, smelted margins have enhanced porosity in the form of many small voids interspersed with metallic particles within the smelted olivine domains (Figs. 2D, 5). NWA 7630 has extensive porosity associated with smelting (Fig. 5A), whereas others has less intense but still well-developed porosity (Figs. 2D, 5B), and some have glass or SiO_2-filled porosity (Figs. 5A). In NWA 11755, all pyroxenes contain abundant large pores (Fig. 5C; see equivalent in Warren and Rubin, 2010), and all smelted domains are highly porous. Fine-grained ureilites are also highly porous, and equivalent ureilites have been described previously (e.g., Herrin et al., 2010; Zolensky et al., 2010; Horstmann and Bischoff, 2014).

Some of ureilites have smelted margins with delicate plume-like structures (Fig. 1A-C), whereas several ureilites show a strong association between smelting and annealing (Fig. 6; see additional examples in Rubin, 2006; Warren and Rubin, 2010). NWA 2705 appears to contain at least two generations of smelting (Fig. 6). The first is associated with irregular patches containing higher abundance of graphite + elongated diamond, and is distinctive for its

261 closely spatially-tied coarse annealing of shock-twinned olivine with granular polygonal (i.e.,
262 well-equilibrated) sub-grains up to 70 μm across and metal + troilite between the sub-grains.
263 The second has delicate plumose and more sulfur-rich smelting textures along metal-troilite-
264 graphite veins with no associated annealing. The metal–troilite particles in the first smelted-
265 annealed domain are distinctly coarser than in the second domain (Fig. 6B).
266
267 The olivine grains in NWA 5996 and NWA 7983 are entirely annealed. In these, the texture is
268 akin to that described for the fine-grained porous ureilites of Almahatta Sitta (Fig. 6E; compare
269 with figure 7 in Horstmann and Bischoff, 2014), which have typically been pervasively reduced
270 (Zolensky et al., 2010; Herrin et al., 2010). We refer to fine-grained texture as whole-sample
271 annealing, because the outlines of large pre-existing olivine grains are clearly visible.
272 Annealing must have occurred at high temperatures because pigeonite and evidence of silicate
273 melting are found in the fine-grained assemblage (see also Warren and Rubin, 2010).
274
275 Under high T-P equilibrium conditions, graphite would be expected to sit along the silicate
276 grain boundaries, either as individual crystals or as isolated inclusions in the olivine and
277 pyroxene, and this equilibrium texture is seen in some ureilites (e.g., Fig. 7A). In contrast, a
278 significant proportion of the graphite + diamond in most samples sits in semi-continuous and
279 sometimes highly irregular veins and vein-networks that cut across the silicate minerals (Fig.
280 7B-C), indicating that extensive carbon migration occurred in many ureilites (see also Day et
281 al., 2017; Rai et al., 2020). Careful observation of most coarse-grained ureilites reveals that
282 varying proportions of the carbon (0-100%) sits in similarly transgressive settings (Table 1;
283 Figs. 2A and B, 6), and at a larger scale, the abundance of carbon varies significantly across
284 thin sections (notably NWA 11754) and between samples.
285

Table 1 has been arranged in order of increasing fayalite content to allow examination of whether there is any correlation between primary olivine composition and the various features noted. Our observations were unable to detect any relationships between olivine Fa content and extent of smelting, extent or proportion of sulfidation, proportion of transgressive carbon veining, or presence or absence of annealing.

Redox modelling

Figure 8 shows the results of the redox modelling. Because the FeO concentration in olivine and pyroxene varies considerably in ureilites (Berkley et al., 1980; Goodrich et al., 2015), several models are presented to cover the range of compositions. Modelling in the C-O-H system shows that the CH_4-C buffer occurs at significantly lower fO_2 than the C-CO buffer. The reaction has been plotted for increasing $X(H_2O)$, from pure CH_4 to 20 mol.% H_2O, and shows that this reaction occurs at progressively more oxidised conditions as $X(H_2O)$ increases. Figure 8A, calculated at 100 bar pressure, shows that only the most oxidised olivine chemistries (the most FeO-rich) can be slightly reduced by the C-CO buffer at nearly 1300°C. At this pressure, the extremely reduced olivine and orthopyroxene compositions found in smelted domains (the blue line labelled Fa_1Fs_3) cannot be formed by C-CO-driven reduction. In Figure 8B, drawn at 1000 bar pressure, none of the olivine chemistries found in ureilites can be reduced by the C-CO buffer. In distinct contrast, a methane-dominated fluid can drive reduction of olivine to the observed FeO-depleted state even at modest temperature and 1000 bar. The positions of the C-CO and CH_4-C buffers are significantly shifted to lower fO_2 conditions at 100 bar relative to the OPI buffer because gases are significantly affected by pressure, whereas solids are not.

311

312

313 **Decompression calculations**

314

315 Figure 9 shows the results of the adiabatic decompression calculations. It can be seen that there
316 is an exponential decrease in the temperature of the gas as pressure drops, with a very large
317 decrease from 200 to 1 bar. The final temperature of the gas is modelled to be 218°C at 1 bar
318 (down from 1280°C at 1000 bar) from isentropic cooling alone. The effect of this strong
319 cooling on the temperature of the coexisting silicates is complex and has not been modelled,
320 but it will be primarily a function of the proportion of gas/fluid to solid/melt (higher gas/fluid
321 abundance = greater cooling effect), which is unconstrained and likely to be variable between
322 samples.

323

324 The gas partitioning calculations show that there are large exponential decreases in the
325 solubility of all volatiles in the silicate melt with decompression (Supp. Data). At peak P-T
326 conditions, there can be several percent volatiles dissolved in the silicate melt, and since the
327 dissolved component is dominated by H_2O, this is a strong function of fH_2O/fCO_2. Given the
328 low fO_2, H_2S and S_2 strongly predominate over SO_2 in the gas phase at all P-T and fH_2O/fCO_2
329 conditions and bulk compositions considered. Changing the bulk composition from basaltic to
330 rhyolitic in *D-Compress* (i.e., simulating SiO_2 addition to the melt; cf. Fig. 4) causes an increase
331 in the H_2O concentration in the silicate melt, and a decrease in the S concentration, with inverse
332 changes to these in the coexisting gas. An important observation is that as fH_2O/fCO_2
333 decreases at fixed P-T conditions and bulk composition, the concentrations of $S_2 + H_2S$ in the
334 gas phase increases (Fig. 10). Conversely, the concentrations of $H_2 + CH_4$ in the gas phase
335 increase with increasing fH_2O/fCO_2 (the abundance of H_2 far exceeds CH_4 at all conditions

investigated). These relationships apply at high and low pressures, and so are maintained in a decompressing system.

DISCUSSION

We do not dispute that the UPB was catastrophically disrupted at high temperature because nearly all ureilites contain uninverted pigeonite, including fine-grained ureilites, and therefore must have cooled rapidly from temperatures of 1200-1300°C (Herrin et al., 2010; Mikouchi et al., 2010; Horstmann and Bischoff, 2014). Thus, graphite-driven smelting, which requires high temperature at very low pressures (e.g., Warren and Huber, 2006), is likely to have been ubiquitous, creating a system with widespread CO gas. However, we aim to show below that it was not the only reduction mechanism operating. In this discussion, we will focus on providing evidence that percolation of a more complex gas/fluid drove varying proportions of secondary smelting.

Pre-disruption conditions within the UPB

Olivine cores in ureilites contain 3 to 26 mol.% fayalite (Goodrich et al. 2004; Downes et al., 2008; Goodrich et al., 2015), a larger range than any other equilibrated primitive meteorite group (Tomkins et al., 2020). The primary smelting model was an early explanation for this variation, whereby FeO was variably reduced to metal by oxidation of graphite to CO at low pressure during high temperature melting (Singletary and Grove 2003; Goodrich et al. 2004, 2007; Wilson et al. 2008). However, the correlation between $\delta^{13}C$ and olivine FeO indicates

clearly that primary smelting did not occur (Barrat et al., 2017), and thus ureilites formed at > 150 bar (cf. Collinet and Grove 2020). On this basis, our calculations suggest that the UPB diameter may have been > 534 km: at this size the uppermost mantle is at 150 bar and the pressure at the core-mantle boundary would be ~1200 bar (Supp. Data, which also contain an analysis for LL chondrites). This minimum diameter was calculated assuming 20% silicate melt extraction to the crust, and core size and composition equivalent to metal-troilite content of H chondrites (selected because Goodrich et al., 2013b suggested that the pre-metamorphic composition of ureilites was metal rich). The diameter would be > 620 km for 15% silicate melt extraction. Note that this is a conservative minimum estimate and thus the UPB was likely a dwarf planet, given that 525 km Vesta verges on being classed as such. The Sanders et al. (2017) hypothesis of isotopic mixing through pre-anatectic H_2O-driven oxidation provides a plausible explanation for the FeO variation that would work within a larger body where smelting is inhibited (given the abundant carbon in ureilites, the initial UPB was likely volatile rich).

As metamorphic temperature increased, silicate melting would have consumed some of the H_2O budget, increasing with depth; basaltic melt at 1280°C and 200 bar would dissolve 1.04 wt% H_2O, whereas at 1200 bar it would dissolve 3.07 wt% H_2O (at high H_2O/CO_2). Given that the melt fraction may have been on the order of 20%, it is plausible that at shallow levels in the UPB mantle there was excess H_2O at peak P-T conditions (e.g., 20% of 1.04 is 0.21 wt% H_2O). Nonetheless, extraction of most of the silicate melt to the crust would be expected to remove much of the initial H_2O budget.

Some silicate melt appears to have been retained within the UPB mantle, as evidenced by the partially crystallized silicate glass encapsulating metal-troilite globules found along grain

boundaries (Fig. 3D) in most ureilites. Comparable grain-boundary veinlets in an augite-bearing ureilite were interpreted by Rosen et al. (2019) as primary melts, and we concur with their suggestion that they occur in many ureilites (70% of our ureilite samples contain trace to minor proportions of these grain boundary veinlets). Smelting produces SiO_2 (detail below), so cannot explain the relatively mafic compositions seen in these glass + crystal veins. They also cannot be the product of decompression melting after complete melt extraction because the glasses contain significant proportions of Al_2O_3, Na_2O and minor K_2O (Supp. Data), which are not sufficiently available from the residual silicates. Further evidence that some primary silicate melt remained is provided by the encapsulated elongate metal-troilite globules. Metal-sulfide melt has much higher density, much lower viscosity and lower solidus temperature than silicate melts. Combined, these factors mean that they are more efficiently segregated during core formation than silicate melts. However, because metal-sulfide melts do not wet residual silicates, whereas silicate melts do, the former tend to migrate along interconnected silicate melt pathways and then become trapped between residual silicates as the silicate melt fraction drops to a few percent, somewhat choking the melt network, promoting entrapment of silicate melt (Tomkins et al., 2020). Thus, partial retention of the metal-troilite melt assemblage along grain boundaries, and the co-existence of silicate melt in these sites, implies that primary silicate melt was partially retained. Because the wetting properties of silicate melt cause it to become thinly dispersed along grain boundaries and triple junctions, initial crystallization via overgrowth of existing silicates (Fig. 3D; Tait et al., 2014) obscures evidence of the melt network, so retention of primary melt would have been greater than is typically apparent from petrographic analysis. The low gravity environment also makes it unlikely that extraction was 100% efficient.

At peak P-T conditions immediately before impact disruption, a small proportion of CHOS fluid should have been dissolved in the retained primary silicate melt, more so at greater depths. Decompression would have caused this volatile component to be exsolved from the melt. Rounded voids suggestive of exsolved volatiles are common in the silicate glass veinlet networks (Figs. 3a, c). The observed large range of polyaromatic hydrocarbon phases coexisting with diamond and graphite in ureilites (e.g., Glavin et al., 2010; Le Guillou et al., 2010), indicates that H was present after peak temperature in the ureilites.

Post-disruption gas/fluid-rock interaction within the UPB

The observations of this study clearly show that smelting in ureilites was not constrained to grain boundaries, but commonly also occurred on fractures away from grain-boundary graphite (Figs. 1-3). These fractures propagate well into olivine grains, commonly crosscutting them entirely, and imply that a gas- and/or fluid-borne phase was responsible for much of the smelting. If smelting were only caused by graphite oxidation in solid-state Reactions 1 and 2 after disruptive impact, smelting should occur everywhere that olivine and graphite are in contact, not in localized domains. In contrast, because gas/fluid-induced smelting would be dependent on migration paths, the extent of smelting would vary as a function of gas/fluid flux and thus permeability, as observed in the hierarchical correlation between fracture size and smelting intensity (Figs. 1, 3F, 9). The textures imply a predominance of gas/fluid-associated smelting over graphite-associated smelting in many samples.

Further support for the notion of gas/fluid migration through ureilites is given by their unusually high noble gas contents compared to other achondrites (e.g., Rai et al., 2003). The

observed formation of troilite within the fracture-hosted smelting texture (Fig. 2) also *requires* addition of gas/fluid-borne sulfur to those sites; calculations indicate that S_2 dominates over H_2S at very low fH_2O/fCO_2, whereas H_2S is predominant at modest fH_2O/fCO_2 (Fig. 10). The observation of carbon in some smelting-associated fractures cutting primary olivine (Figs. 2A, 6A and C; Table 1) and pyroxene (Fig. 7B-D) imply that carbon was mobilized and precipitated after peak metamorphic equilibration. To explain this observation, the gas/fluid phase would also need to contain a carbon-bearing component, perhaps primarily CH_4, and perhaps evolving to a large array of hydrocarbons during cooling. Thus, a C-H-O-S gas/fluid likely played a role in secondary smelting in most ureilites.

The plume-like textures typical of grain-boundary and fracture-hosted smelted regions (Fig. 1) are not characteristic of solid-state reactions, which rely on element diffusion through the olivine crystal structure and would generate even diffusion gradients at all graphite-olivine interfaces (Khawam and Flanagan, 2006). Putnis (2009) described numerous examples of mineral replacement textures produced by fluid-rock interaction – known as coupled dissolution-reprecipitation (CDR) – which is common in hydrothermal systems on Earth. A ubiquitous characteristic of fluid-mediated mineral replacement is the presence of fine porosity in the replacing phase, generated because the ΔV of reaction is negative. This volume change enhances fluid penetration to the replacement front and allows exchange and removal of components at the reaction interface. Irregular replacement textures develop because reaction is enhanced at areas of irregularity in the crystal lattice. The observed plume-like smelting textures in the ureilites, with their distinct porosity (Fig. 5B) and the presence of fine-grained metal and troilite (Figs. 1, 2, 4), along with molar volumes decreasing from fayalite > forsterite >> enstatite >> quartz, are diagnostic of fluid- or gas-mediated CDR mineral replacement (cf.

459 Ahmad et al., 2014). Note also that the presence of porosity in this setting does not require or
460 exclude the presence of gas.
461
462 The fact that even the smallest fractures, < 50 μm in length, are bordered by reduced olivine
463 (Fig. 1A) implies that the system maintained elevated gas/fluid pressure to drive the reactants
464 into all available fractures and porosity (i.e., the system did not satisfy the thermodynamic
465 definition of free expansion). This high gas/fluid pressure could be explained by gas/fluid
466 production during smelting (as suggested previously; e.g., Warren and Rubin, 2010), and/or by
467 expansion of the gas/fluid exsolving from silicate melt as pressure dropped upon UPB
468 disruption. Regarding the latter, the gas/fluid evolution in the UPB system during impact
469 disruption can be conceptualized as being broadly equivalent to the fluid > gas evolution in an
470 erupting volcanic system on Earth; that is, starting with supercritical fluid at modest pressure
471 in equilibrium with silicate melt + crystals then rapidly evolving to gas at low pressure.
472
473 In volcanic systems on Earth, fluid-gas expansion as magmas rise through the uppermost crust
474 causes cooling on the order of several hundred kelvin (e.g., Shinohara et al., 2018). The
475 considerable cooling that would be experienced by the gas phase during catastrophic
476 decompression of the UPB (Figure 9) suggests that it may be capable of rapidly cooling the
477 silicate assemblage below the blocking temperature of Ca-Fe-Mg diffusion in pigeonite, which
478 is on the order of 900°C (Tomkins et al., 2020). Given that smelting textures are widely
479 distributed at very fine scale throughout all ureilites – some much more extensively than others
480 – the gas phase would have been pervasively distributed, which would maximise the adiabatic
481 cooling effect during decompression. It has previously been suggested that all UPB fragments
482 sampled by meteorites were very small, based on the idea that extremely rapid cooling is
483 achieved by radiative heat loss (e.g., <10 m diameter: Herrin et al., 2010). However, adiabatic

484 cooling may explain why rapid cooling is seen in all ureilites, whilst allowing for the existence
485 of larger UPB fragments.
486
487 Several ureilites examined in this study are either fully annealed (NWA 5996, NWA 7983) or
488 have domains of annealing associated with smelting (NWA 2705, NWA 4471, NWA 11755)
489 (see also Rubin, 2006). Additionally, the fine-grained ureilites of the Almahatta Sitta fall (28.4%
490 of the ureilitic samples) appear to be equivalent to NWA 5996 and NWA 7983 based on the
491 descriptions in Zolensky et al. (2010), Warren and Rubin (2010) and Horstmann and Bischoff
492 (2014), and thus also represent fully annealed ureilites. Warren and Rubin (2010) suggested
493 that annealing implies that the affected meteorites remained hotter for longer than the ureilites
494 that have delicate plumose smelting. However, if a supercritical fluid or a higher density gas
495 was present at the earliest stages of decompression, this would tend to drive rapid annealing
496 because fluids are highly effective at driving recrystallization through enhancing diffusion
497 (Aradi et al., 2017; Zhao et al., 2017). We infer that annealing was facilitated by gas/fluid
498 infiltration associated with smelting, based on the vein-like carbon distribution (Fig. 6) and the
499 observed intimate relationship between the distribution of smelting and annealing that transects
500 the primary fabric. Smelting is interpreted to have occurred during annealing because the
501 annealed domains have Fe-depleted olivine and metal grains decorating sub-grain boundaries
502 (Fig. 6). The two-staged smelting in NWA 2705 (Fig. 6) implies an initial smelting and
503 annealing process, perhaps involving a denser gas/fluid, and a later stage of delicate plumose
504 smelting associated with a gas. For a supercritical fluid or dense gas phase to be present, the
505 pressure inside some UPB fragments would need to be above or close to the critical pressure
506 for the relevant gas mix. The higher pressures required by both slow cooling-associated
507 annealing, and by denser gas/fluid-associated annealing, imply that the gas/fluid component

508 driving the annealing+smelting was more reduced than graphite (since Reactions 1 and 2 are
509 inhibited by increased P).
510
511
512 **Gas/fluid-borne reductants**
513
514 Given that a high proportion of ureilites contain transgressive veinlets and vein-network arrays
515 of graphite + diamond, a mechanism is needed to explain the implied carbon mobilization.
516 Methane is the stable hydrocarbon phase at the high P-T and reduced conditions of large
517 asteroid and rocky planet mantles (cf. Lobanov et al., 2013). The silicate melt equilibration
518 calculations indicate that H_2 is expected to be an abundant gas species at modest fH_2O/fCO_2
519 conditions (Fig. 10). Another possible source of H_2 is the metal-sulfide melt, which has been
520 experimentally shown to dissolve small quantities of H_2 (Kubaschewski, 2013). As a strong
521 reducing agent, H_2 is expected to react with graphite, producing methane:
522
523 $2H_2 + C = CH_4$ [5]
524
525 It would also be effective at reducing olivine to Fe metal, and experiments have shown that Fe-
526 Ni metal catalyses methane formation in H_2-CO_2 mixtures (Reeves and Fiebig, 2020). It is
527 therefore proposed that the gas/fluid that caused this smelting was methane- and H_2-bearing.
528 Methane and H_2 could produce the observed smelting textures, the carbon vein arrays and the
529 SiO_2 production through a combination of the following reactions:
530
531 $H_2 + FeMgSiO_4 = MgSiO_3 + Fe + H_2O$ [6]
532

533 $2H_2 + 2FeMgSiO_4 = Mg_2SiO_4 + SiO_2 + 2Fe + 2H_2O$ [7]

534

535 $CH_4 + 2FeMgSiO_4 = 2MgSiO_3 + 2Fe + C + 2H_2O$ [8]

536

537 $CH_4 + 2FeMgSiO_4 = Mg_2SiO_4 + SiO_2 + 2Fe + C + 2H_2O$ [9]

538

539 The sulfur addition that is widespread in smelted domains (Fig. 2) is explained by gas/fluid-
540 driven reactions:

541

542 $3S_2 + 4FeMgSiO_4 = 4MgSiO_3 + 4FeS + 2SO_2$ [10]

543

544 $3S_2 + 4FeMgSiO_4 = 2Mg_2SiO_4 + 2SiO_2 + 4FeS + 2SO_2$ [11]

545

546 $H_2S + FeMgSiO_4 = MgSiO_3 + FeS + H_2O$ [12]

547

548 $2H_2S + 2FeMgSiO_4 = Mg_2SiO_4 + SiO_2 + 2FeS + 2H_2O$ [13]

549

550 The H_2S and S_2 for these reactions would result from the breakdown of FeS to Fe that occurs
551 at high temperatures (e.g., Tomkins, 2009), with H_2S formation promoted by decompression
552 as H_2O exsolves from the silicate melt, increasing H_2O/CO_2 (Fig. 10). Excess S_2 and H_2S
553 migrating through low sulfur domains is expected to promote sulfidation of metal, and thereby
554 melting of metal+troilite, for example:

555

556 $S_2 + 2Fe = 2FeS \quad > \quad Fe + FeS = melt \quad (at\ T > 988°C)$ [14]

557

$H_2S + Fe = FeS + H_2$ > $Fe + FeS = melt$ (at T > 988°C) [15]

$2H_2S + 2Fe + C = 2FeS + CH_4$ > $Fe + FeS = melt$ (at T > 988°C) [16]

Because carbon is a product of some of the above reactions, they offer a more satisfactory explanation for the observed carbon veins (Fig. 7; Table 1), and the intermixing of FeS amongst this vein graphite, than the carbon-consuming Reactions 1 and 2. Reactions can also be written for gas phases like carbonyl sulfide (OCS) and carbon disulfide (CS_2) and these are expected to be minor components of a gas/fluid system that would have varied significantly in its proportion of components as it cooled, for example:

$Fe + CS_2 = FeS + C$ [17]

The relative prevelance of the carbon-producing reactions would depend on the $X(H_2O)$ of the gas/fluid driving the reaction, and on the temperature of the system. The observations that the smelted silicate product consists primarily of forsterite, and Si-rich melt is present in many examples, implies that Reactions 7, 9, 11 and 13 may be dominant, although orthopyroxene was produced (i.e., Reactions 6, 8, 10 and 12) in some instances. Textures like those in Figure 3C-E, involving reduction of pyroxene, are best explained by reactions like:

$H_2 + FeMgSi_2O_6 = MgSiO_3 + SiO_2 + Fe + H_2O$ [18]

$CH_4 + 2FeMgSi_2O_6 = 2MgSiO_3 + 2SiO_2 + 2Fe + C + 2H_2O$ [19]

$3S_2 + 4FeMgSi_2O_6 = 4MgSiO_3 + 4SiO_2 + 4FeS + 2SO_2$ [20]

583

584 $H_2S + FeMgSi_2O_6 = MgSiO_3 + SiO_2 + FeS + H_2O$ [21]

585

586 The compositions of the silicate melt present in most ureilites imply that a small amount of
587 melt was present at peak P-T conditions: they are relatively rich in Na, which is not available
588 in sufficient quantities from the pyroxene or olivine. Additional melt (e.g., Fig. 3A) was likely
589 generated through co-production of H_2O and SiO_2 upon decompresion and initiation of
590 smelting, producing the SiO_2 enrichment trend seen amongst the melt compositions (Fig. 4).
591 This felsification of the silicate melt would tend to consume H_2O and thereby somewhat buffer
592 the coexisting fluid towards lower $X(H_2O)$.

593

594 Figure 8 indicates that the olivine typically found in ureilites would be smelted by a CH_4-rich
595 fluid, at temperatures far lower than required for graphite-driven smelting, even at deep mantle
596 pressures. At 100 bar, some graphite-driven smelting could only occur above 1290°C, but only
597 involving the most oxidised ureilite olivine grains (Fig. 8A), and would produce olivine with
598 much higher FeO content than those observed in smelted domains. These results are consistent
599 with the consensus view that graphite-driven olivine reduction can only work when the UPB
600 is disrupted into small fragments (e.g., Warren, 2012). In contrast, a low H_2O, CH_4-rich fluid
601 (high proportions of H_2S are allowable; see below) is capable of reaching the necessary
602 conditions in all ureilite compositions at temperatures as low as 800°C at 1000 bar, and as low
603 as 700°C at 100 bar. The H_2O-producing reactions would tend to buffer $X(H_2O)$ to the limit of
604 that needed for smelting. However, by creating a more reduced assemblage along the margins
605 of the gas/fluid pathway, the system would progressively evolve a permeable network
606 chanellized by non-reactive smelted margins that cannot buffer $X(H_2O)$, along which reduced
607 gas/fluid could migrate into unreacted rock.

608

609 The porosity created by the smelting process, and by the large volume expansion in the
610 decompressing gas/fluid, would drive continued smelting along the gas/fluid network,
611 particularly in areas of high fracture density. The volume of rock affected by this process would
612 then be limited by the availability of H_2, CH_4, S_2 and H_2S, and eventually by temperature. In
613 this scenario, high fluid flux domains would be more intensely affected by smelting than low
614 flux regions. This relationship is common in the ureilites examined. Within individual samples
615 there are some domains where there are broad regions of intense smelting, and narrow regions
616 of mild smelting, and this commonly scales proportionally with the size of the fractures and
617 grain boundary length (i.e., smaller microfractures tend to have thinner smelted domains; Figs.
618 1, 2). Comparisons between ureilites also show that some are significantly more affected by
619 smelting than others.

620

621 In addition, the $X(H_2)$ and $X(CH_4)$ of the fluid can also be buffered by iron sulfide formation
622 in smelted domains, through Reactions 15 and 16 (reacting with the small metal particles in
623 smelting domains). Because these reactions increase $X(H_2)$ and $X(CH_4)$, they maintain the
624 reduced state of the fluid and thus enhance the smelting process *in situ*. Thus, there would be
625 a positive feedback effect when H_2S is an important fluid species together with CH_4; the
626 reduction of olivine frees iron to react with the H_2S and catalyse conversion of C to CH_4.
627 Consequently, Reactions 6-21 would be coupled, and this is consistent with the observed
628 troilite in the smelted domains of all ureilites (Table 1), exemplified in Figures 1 and 2. Thus,
629 the ideal gas/fluid for widespread fracture-associated smelting consists of H_2 + CH_4, a
630 significant proportion of S_2 + H_2S, and low H_2O, although H_2O can be removed by felsification
631 of the silicate melt, and/or reaction with carbon during cooling to form the hydrocarbons
632 reported in ureilites (e.g., Glavin et al., 2010; Le Guillou et al., 2010).

633

634 The positive correlation between $(H_2+CH_4)/(H_2S+S_2)$ and fH_2O/fCO_2 in the decompression
635 modelling (Fig. 10), implies that high FeNi metal/troilite ratios in some smelted domains
636 indicates higher fH_2O/fCO_2 (and H_2 and CH_4) in those parts of the decompressing system.
637 And, abundant troilite in other domains implies low fH_2O/fCO_2 and high H_2S and S_2 there.
638 Given that ureilites contain considerable variation in relative abundance of smelting-associated
639 Fe metal and troilite, as well as large variability in smelting intensity and carbon vein-network
640 overprinting, the abundance and composition of gas/fluid must have been very heterogeneous
641 within the UPB as it decompressed.

642

643

644 **CONCLUSIONS**

645

646 The presence of fracture-hosted smelted domains within olivine and pyroxene, the abundant
647 troilite and porosity amongst metal in these domains, and widespread plume-like reaction fronts,
648 indicate that some form of highly reduced gas or fluid moved through the ureilite parent body
649 and drove a considerable proportion of secondary smelting, in some samples the dominant
650 majority. The extent of smelting varied as a function of gas/fluid flux, such that micro-domains
651 of greatest flux were the most extensively smelted. The most effective way to generate
652 widespread smelting is through migration of gas/fluid with abundant H_2, CH_4, S_2 and H_2S, with
653 low H_2O. Reactions involving these CHOS components provide an explanation for the
654 presence of transgressive carbon veins, the addition of sulfur to smelted domains and the
655 presence of hydrocarbons in ureilites despite peak metamorphic temperatures approaching
656 1300ºC. The CHOS components may have been released from the syn-peak melt upon
657 decompression after a catastrophic impact. Smelting-associated annealing may have been

promoted by a high-density gas or supercritical liquid in higher-pressure domains within larger UPB fragments. Some ureilites preserve an early stage of smelting-associated annealing overprinted by fracture-associated smelting with delicate plumose reaction fronts, implying an evolution from supercritical liquid to gas, consistent with progressive decompression and cooling, or perhaps associated with sequential impacts. Rapid cooling was at least partially achieved by adiabatic cooling of the expanding gas phase. A broader implication of our findings is that if a dwarf planet starts out being volatile rich, its mantle will retain a range of volatiles, despite considerable melt extraction, unless disrupted by a catastrophic impact.

ACKNOWLEDGEMENTS

Electron microscopy was performed at the Monash Centre for Electron Microscopy, the CSIRO Microbeam Laboratory and the Plymouth Electron Microscopy Centre. Hilary Downes and an anonymous reviewer and associate editor Kevin Righter are thanked for their efforts in reviewing the manuscript, which helped to improve the final product. The authors declare no conflict of interest.

AUTHOR CONTRIBUTIONS

A.D.L. wrote initial drafts of the paper and conducted some of the petrology work as part of his PhD studies. A.G.T. conceptualized and supervised the project, conducted much of the petrology work and rewrote the paper. K.A.E. performed the thermodynamic calculations. N.C.W., C.M., A.T., and N.R.S. were integral to the electron microscopy work.

683

684 **REFERENCES**

685

686 Ahmad, S., Rhamdhani, M. A., Pownceby, M. I. and Bruckard, W. J. (2014) Thermodynamic
687 assessment and experimental study of sulphidation of ilmenite and chromite. *Min. Proc.*
688 *Extract. Metal.* **123**, 165-177.

689 Aradi, L. E., Hidas, K., Kovacs, I. J., Tommasi, A., Klebesz, R., Garrido, C. J. and Szabo, C.
690 (2017) Fluid-enhanced annealing in the subcontinental lithospheric mantle beneath the
691 westernmost margin of the Carpathian-Pannonian extensional basin system. *Tectonics* **36**,
692 2987-3011.

693 Barrat, J.-A., Sansjofre, P., Yamaguchi, A., Greenwood, R. C. and Gillet, P. (2017) Carbon
694 isotopic variation in ureilites: Evidence for an early, volatile-rich inner Solar System. *Earth*
695 *Planet. Sci. Lett.* **478**, 143-149.

696 Berkley, J. L. and Jones, J. H. (1982) Primary igneous carbon in ureilites: petrological
697 implications. *J. Geophys. Res. Solid Earth* **87**, A353-A364.

698 Berkley, J. L., Taylor, G. J., Keil, K., Harlow, G. E. and Prinz, M. (1980) The nature and origin
699 of ureilites. *Geochim. Cosmochim. Acta* **44**, 1579-1597.

700 Broadley, M. W., Bekaert, D. V., Marty, B., Yamaguchi, A. and Barrat, J.-A. (2020) Noble gas
701 variations in ureilites and their implications for ureilite parent body formation. *Geochim.*
702 *Cosmochim. Acta* **270**, 325-337.

703 Burgisser, A., Alletti, M. and Scaillet, B. (2015) Simulating the behavior of volatiles belonging
704 to the C–O–H–S system in silicate melts under magmatic conditions with the software D-
705 Compress. *Computers Geosci.* 79, 1–14.

706 Collinet, M. and Grove, T. L. (2020) Incremental melting in the ureilite parent body: Initial
707 composition, meltingtemperatures, and melt compositions. *Meteorit. Planet. Sci.* **55**, 832-
708 856.
709 Day, J.M., Corder, C.A., Cartigny, P., Steele, A., Assayag, N., Rumble III, D. and Taylor, L.A.
710 (2017) A carbon-rich region in Miller Range 091004 and implications for ureilite
711 petrogenesis. *Geochim. Cosmochim. Acta* **198**, 379-395.
712 Downes, H., Mittlefehldt, D. W., Kita, N. T. and Valley J. W. (2008) Evidence from polymict
713 ureilite meteorites for a disrupted and re-accreted single ureilite parent asteroid gardened by
714 several distinct impactors. *Geochim. Cosmochim. Acta* **72**, 4825–4844.
715 Franchi, I. A., Baker, L., Bridges, J. C., Wright, I. P. and Pillinger, C. T. (2001) Oxygen
716 isotopes and the early solar system. *Phil. Trans. Royal Soc. London, Series A* **359**, 2019–
717 2035.
718 Glavin, D. P., Aubrey, A. D., Callahan, M. P., Dworkin, J. P., Elsila, J. E., Parker, E. T., Bada,
719 J. L., Jenniskens, P. and Shaddad, M. H. (2010) Extraterrestrial amino acids in the Almahata
720 Sitta meteorite. *Meteorit. Planet. Sci.* **45**, 1695–1709.
721 Goodrich, C. A. (1992) Ureilites: A critical review. *Meteoritics* **27**, 327-352.
722 Goodrich C. A., Ash R. D., Van Orman J. A., Domanik K., and McDonough W. F. (2013b)
723 Metallic phases and siderophile elements in main group ureilites: Implications for ureilite
724 petrogenesis. *Geochimica Cosmochim. Acta* **112**, 340–373.
725 Goodrich, C. A., Hartmann, W. K., O'Brien, D. P., Weidenschilling, S. J., Wilson, L., Michel,
726 P. and Jutzi, M. (2015) Origin and history of ureilitic material in the solar system: The view
727 from asteroid 2008 TC3 and the Almahata Sitta meteorite. *Meteorit. Planet. Sci.* **50**, 782-
728 809.

729 Goodrich, C. A., Jones, J. H. and Berkley, J. L. (1987) Origin and evolution of the ureilite
730 parent magmas: Multi-stage igneous activity on a large parent body. *Geochim. Cosmochim.*
731 *Acta* **51**, 2255–2273.
732 Goodrich, C. A., Scott, E. R. D. and Fioretti, A.M. (2004) Ureilitic breccias: Clues to the
733 petrologic structure and impact disruption of the ureilite parent asteroid. *Chemie der Erde*
734 **64**, 283–327.
735 Goodrich C. A., Sutton, S. R., Wirick, S. and Jercinovic, M.J. (2013a) Chromium valences in
736 ureilite olivine and implications for ureilite petrogenesis. *Geochimica Cosmochim. Acta* **122**,
737 280–305.
738 Goodrich, C. A., Van Orman, J. A., Wilson, L. (2007) Fractional melting and smelting on the
739 ureilite parent body. *Geochim. Cosmochim. Acta* **71**, 2876-2895.
740 Herrin, J. S., Zolensky, M. E., Ito, M., Le, L., Mittlefehldt, D. W., Jenniskens, P., Ross, A. J.
741 and Shaddad, M.H. (2010) Thermal and fragmentation history of ureilitic asteroids:insights
742 from the Almahata Sitta fall. *Meteorit. Planet. Sci.* **45**, 1789–1803.
743 Holland, T. J. B. and Powell, R. (2011) An improved and extended internally consistent
744 thermodynamic dataset for phases of petrological interest, involving a new equation of state
745 for solids. *J. Met. Geol.* **29**, 333-383
746 Horstmann, M. and Bischoff, A. (2014) The Almahata Sitta polymict breccia and the late
747 accretion of asteroid 2008TC3. *Chemie der Erde* **74**,149–183.
748 Khawam, A. and Flanagan, D.R. (2006) Solid-state kinetic models: Basics and mathematical
749 fundamentals. *J. Phys. Chem. B* **110**, 17315-17328.
750 Kita, N. T., Ikeda, Y., Togashi, S., Liu, Y., Morishita, Y. and Weisberg, M. K. (2004) Origin
751 of ureilites inferred from a SIMS oxygen isotopic and trace element study of clasts in the
752 Dar al Gani 319 polymict ureilite. *Geochim. Cosmochim. Acta* **68**, 4213-4235.

753 Kojima, T. and Tomeoka, K. (1996) Indicators of aqueous alteration and thermal
754 metamorphism on the CV parent body: Microtextures of a dark inclusion from Allende.
755 *Geochim. Cosmochim. Acta* **60**, 2651-2666.
756 Kubaschewski, O. (2013) Iron—Binary phase diagrams. Springer Science & Business Media.
757 185p.
758 Le Guillou, C., Rouzaud, J. N., Remusat, L., Jambon, A., Bourot-Denise, M. (2010) Structures,
759 origin and evolution of various carbon phases in the ureilite Northwest Africa 4742
760 compared with laboratory-shocked graphite. *Geochim. Cosmochim. Acta* **74**, 4167-4185.
761 Lobanov, S. S., Chen, P.-N., Chen, X.-J., Zha, C.-S., Litasov, K. D., Mao H.-K. and Goncharov,
762 A.F. (2013) Carbon precipitation from heavy hydrocarbon fluid in deep planetary interiors.
763 *Nature Com.* **4**, 2446.
764 MacRae, C.M., Wilson, N.C. and Torpy, A. (2013) Hyperspectral cathodoluminescence. *Miner.*
765 *Petrol.* 107, 429–440.
766 Mikouchi, T., Zolensky, M. E., Ohnishi, I., Suzuki, T., Takeda, H., Jenniskens, P. and Shaddad,
767 M. H. (2010) Electron microscopy of pyroxene in the Almahata Sitta ureilite. *Meteorit.*
768 *Planet. Sci.* **45**, 1812–1820.
769 Mittlefehldt D.W., McCoy T.J., Goodrich C.A. and Kracher A. (1998) Non-chondritic
770 meteorites from asteroidal bodies. In: Planetary materials, edited by Papike J. J., Reviews
771 in Mineralogy, vol. 36. Washington, D.C.: Mineralogical Society of America. pp. 4.1–4.195.
772 Putnis, A. (2009) Mineral replacement reactions. *Rev. Min. Geochem.* **70**, 87-124.
773 Rai, N., Downes, H. and Smith, C. (2020) Ureilite meteorites provide a new model of early
774 planetesimal formation and destruction. *Geochem. Perspectives Lett.* **14**, 20-25.
775 Rai, V. K., Murty, S. V. S. and Ott, U. (2003) Noble gases in ureilites: Cosmogenic, radiogenic,
776 and trapped components. *Geochim. Cosmochim. Acta* **67**, 4435-4456.

Reeves, E.P. and Fiebig, J. (2020) Abiotic synthesis of methane and organic compounds in the Earth's lithosphere. *Elements* **16**, 25-31.

Rosen, A.V., Pape, J., Hofmann, B.A., Gnos, E. and Guillong, M. (2019) Quenched primary melt in Ramlat as Sahmah 517 – Snapshot of ureilite anatexis in the early solar system. *Geochim. Cosmochim. Acta* **246**, 1-20

Rubin, A. E. (1988) Formation of ureilites by impact-melting of carbonaceous chondritic material. *Meteoritics* **23**, 333-337.

Rubin, A. E. (2006) Shock, post-shock annealing, and post-annealing shock in ureilites. *Meteorit. Planet. Sci.* **41**, 125-133.

Rubin, A. E. (2012) Collisional facilitation of aqueous alteration of CM and CV carbonaceous chondrites. *Geochim. Cosmochim. Acta* **90**, 181-194.

Sanders, I. S., Scott, E. R. D. and Delaney, J. S. (2017) Origin of mass-independent oxygen isotope variation among ureilites: Clues from chondrites and primitive achondrites. *Meteorit. Planet. Sci.* **52**, 690–708.

Scott, E. R. D., Krot, A. N. and Sanders, I.S. (2018) Isotopic dichotomy among meteorites and its bearing on the protoplanetary disk. *Astrophys. J.* 854:164.

Shinohara, H., Yokoo, A. and Ryunosuke Kazahaya, R. (2018) Variation of volcanic gas composition during the eruptive period in 2014–2015 at Nakadake crater, Aso volcano, Japan. *Earth, Planets Space* **70**, 151.

Singletary, S. J. and Grove, T. L. (2003) Early petrologic processes on the ureilite parent body. *Meteorit. Planet. Sci.* **38**, 95-108.

Sinha, S.K., Sack, R.O., Lipschutz, M.E., 1997. Ureilite meteorites: Equilibration temperatures and smelting reactions. *Geochim. Cosmochim. Acta* **61**, 4235-4242.

Stöffler, D., Keil, K. and Edward, R. D. S. (1991) Shock metamorphism of ordinary chondrites. *Geochim. Cosmochim. Acta* **55**, 3845-3867.

802 Tomkins, A. G. (2009) What metal-troilite textures can tell us about post-impact
803 metamorphism in chondrite meteorites. *Meteorit. Planet. Sci.* **44**, 1133-1149.
804 Tomkins, A. G., Johnson, T. E. and Mitchell, J. T. (2020) A review of the chondrite–achondrite
805 transition, and a metamorphic facies series for equilibrated primitive stony meteorites.
806 *Meteorit. Planet. Sci.* **55**, 857-885.
807 Torpy, A., Wilson, N., MacRae, C., Pownceby, M., Biswas, P., Rahman, M. and Zaman, M.
808 (2020). Deciphering the complex mineralogy of river sand deposits through clustering and
809 quantification of hyperspectral X-Ray maps. *Microscopy Microanal.* **26**, 768-792.
810 Walker, D. and Grove, T. (1993) Ureilite smelting. *Meteoritics* **28**, 629-636.
811 Warren, P.H. (2011) Stable isotopes and the noncarbonaceous derivation of ureilites, in
812 common with nearly all differentiated planetary materials. *Geochim. Cosmochim. Acta* **75**,
813 6912–6926.
814 Warren, P. H. (2012) Parent body depth–pressure–temperature relationships and the style of
815 the ureilite anatexis. *Meteorit. Planet. Sci.* **47**, 209–227.
816 Warren, P. H. and Huber, H. (2006) Ureilite petrogenesis: A limited role for smelting during
817 anatexis and catastrophic disruption. *Meteorit. Planet. Sci.* 41, 835-849.
818 Warren, P. H. and Kallemeyn, G. W. (1992) Explosive volcanism and the graphite-oxygen
819 fugacity buffer on the parent asteroid(s) of the ureilite meteorites. *Icarus* **100**,110–126.
820 Warren, P. H. and Rubin, A.E. (2010) Pyroxene-selective impact smelting in ureilites. *Geochim.*
821 *Cosmochim. Acta* **74**, 5109-5133.
822 Wilson, L., Goodrich, C. A. and Van Orman, J. A. (2008) Thermal evolution and physics of
823 melt extraction on the ureilite parent body. *Geochim. Cosmochim. Acta* **72**, 6154-6176.
824 Zhao, J., Brugger, J., Grguric, B. A., Ngothai, Y. and Pring., A. (2017) Fluid-enhanced
825 coarsening of mineral microstructures in hydrothermally synthesized bornite–digenite solid
826 solution. *ACS Earth and Space Chemistry* **1**, 465-474.

827 Zolensky, M., Herrin, J., Mikouchi, T., Ohsumi, K., Friedrich, J., Steele, A., Rumble, D., Fries,
828 M., Sandford, S., Milam, S., Hagiya, K., Takeda, H., Satake, W., Kurihara, T., Colbert, M.,
829 Hanna, R., Maisano, J., Ketcham, R., Goodrich, C., Le, L., Robinson, G., Martinez, J., Ross,
830 K., Jenniskens, P. and Shaddad, M. H. (2010) Mineralogy and petrography of the Almahata
831 Sitta ureilite. *Meteorit. Planet. Sci.* **45**, 1618-1637.

832

833

834 **Figure Captions**
835
836 **Figure 1.** Non-graphite-related smelting characteristics common to most ureilites. (A-C, BSE
837 images) These images highlight fracture-associated smelting and the typical hierarchy of
838 greater smelting around more dominant fractures. Note also the delicate plumose smelting
839 textures in all three images. The darker zones in olivine indicate areas of Fe depletion. (D,
840 reflected light) A clear difference in the intensity of smelting around a metal-troilite vein (M,
841 metal; S, sulfide) compared to a crystalline graphite grain (G). In this case, the smelting is
842 sulfide-dominated, but this is not always so in this textural setting.
843
844 **Figure 2.** The distribution sulfur in smelted regions in ureilites. (A) A Fe-S-CL map (diamonds
845 in green) highlighting the abundant distribution of fine-grained sulfides in red in all smelted
846 domains (Fe-depleted areas). (B, C) Mg-S maps highlighting abundant sulfide addition
847 associated with smelting. Compare C with Figures 3B and 5. (D, reflected light) Intense
848 sulfidation and associated porosity in NWA 3156.
849
850 **Figure 3.** Silicate melt textures. In (A) an association between olivine and pyroxene smelting
851 and silicate melt formation can be seen, with widely dispersed silicate melt pockets developed
852 within the smelted domain. Metal particles are commonly found in the silicate melt pockets.
853 (B) Si map highlighting the production of high silica minerals/melt during smelting; compare
854 with Figures 2C and 6. (C) Silicate melt filled microfractures cutting pyroxene with narrow Fe-
855 depleted domains at the margins. Metal-troilite melt droplets and veins are typically found
856 within the silicate melt. (D) An example of the textures resulting from crystallisation of primary
857 grain-boundary silicate melt, with glass + euhedral pyroxene crystals and encapsulated globular
858 metal/troilite. (E) A Fe-Si-Mg map highlighting enstatite production associated with olivine
859 smelting, and the subtle smelting around small fractures compared that around large.
860
861 **Figure 4.** Variation in silicate glass compositions in NWA 4471 compared with a vector for
862 SiO_2 addition.
863
864 **Figure 5.** Examples of smelting-associated porosity in ureilites. Some ureilites have
865 extensively developed porosity closely tied to smelted domains such as that shown in (A,
866 reflected light), whereas others have considerably less (compare with Fig. 2D, 3A). (B, BSE)
867 example of the close association between smelted olivine domain and micro-scale porosity. (C,
868 transmitted light) All pyroxenes in NWA 11755 are riddled with inclusions, as shown here,
869 with most consisting of a large void, and some containing sulfides. The olivine in this sample

lacks these inclusions, but is very coarsely annealed, which in turn is overprinted by the same intense porosity as shown in (A).

Figure 6. Different views of the two stages of smelting identified in NWA 2705. Stage 1 smelting has an annealed granular texture amongst clusters of distinctive elongate diamond/lonsdaleite (a CL-bright carbon phase) in graphite (A), with metal decorating the margins of the annealed grains (B). Delicate plumose sulfide-rich smelting (B and C) characterizes the second stage of smelting, focused mainly on fractures cutting olivine. (D, cross polarized light) Olivine sub-grains generated by the smelting-associated annealing are over 200 mm across in some cases. (E, cross polarized light) An example of annealed olivine (the numerous colourful sub-grains) from a pervasively annealed fine grained ureilite, NWA 5996.

Figure 7. Comparison of syn-peak metamorphic graphite with graphite + diamond in semi-continuous veins cutting across poikiloblastic pyroxene. (A, reflected light) A diamond-free ureilite with minimal smelting, preserving the primary peak metamorphic association of crystalline graphite at the grain boundaries of olivine and pyroxene. Metal veins and holes formed by rusting of metal veins are also seen along grain boundaries. (B-C) An example of a transgressive carbon vein in an augite-bearing ureilite. (B, cross polarized light) shows a large primary poikilitic orthopyroxene grain (Opx) with olivine chadacrysts (Ol), with the area of (D) highlighted. (D, reflected light) shows a narrow vein of carbon entirely transgressing the orthopyroxene grain. (C) shows detail of graphite and diamond within the carbon vein, and the highly irregular nature of the vein margins, indicating a high degree of disequilibrium.

Figure 8. Redox buffer curves relevant to smelting of ureilite olivine and pyroxene compositions at 100 bar (A) and 1000 bar (B) confining pressure. Fa_xFs_x numbers indicate the position of Ol-Px-Fe (OPI) oxygen buffer as a function of the proportions of fayalite in olivine and ferrosilite in orthopyroxene. The blue shaded region indicates the position of the OPI buffer for the natural range of pre-smelted olivine and orthopyroxene compositions in ureilites. The light blue line represents the composition of olivine and orthopyroxene observed in smelted regions: this line represents the oxidation state reached by the smelting reaction. Curves labelled X_{H2O} indicate the position of methane-driven smelting for a CH_4-H_2O fluid, indicating systems with nearly pure methane, 5% H_2O and 20% H_2O. It should be noted that H_2S has not been considered for this fluid. The CCO buffer (green line) has been plotted to show smelting without H, allowing a comparison with the oxidation state reached by graphite-driven smelting.

Figure 9. Change in temperature of gas co-existing with silicate melt as a function of pressure decrease.

Figure 10. Variations in the proportions of gases coexisting with basaltic silicate melt as a function of the relative pressures of H_2O and CO_2.

Table 1. Petrographic characteristics of ureilites investigated in this study in order of increasing Fa content.

Name	Silicate Minerals*	Smelting	Carbon Veins	Shock	Mineral elongation	Annealing	Characteristics
NWA 11754	($Fa_{11.4}$), Aug, Opx Igneous cumulate	Weak fracture and grain boundary vein assoc. Sulfide-rich. No graph assoc. smelting	65% of section is carbon free, remainder contains ~5% carbon, of which is 90% irregular transgressive material	Mild: undulose Ol, sparse mosaicism. Sparse microbreccias	Absent	No	2/3 of the section is graphite-free, other 1/3 is has mod. abund. graphite. Numerous fine sulfide±metal filled fractures. Localised sulfide fracture arrays. Chromite-bearing. Sparse silicate melt in fine fractures with sulfides.
NWA 7983	Ol ($Fa_{12.0}$), Pig, Opx	Present, obscured by annealing	100% isolated carbon gains amongst fine-grained annealed silicates	Polished mount only	N/A	100% annealed	Fine-grained porous ureilite. Metal/troilite 95% oxidised.
NWA 4225	Ol ($Fa_{12.7-14.1}$), Pig	Strong. All olivine grain boundaries, porous. Trace sulfide	50% in vein-networks, 50% as large blocks on grain boundaries	Low	Moderate	No	Poikiloblastic Pig wt Ol chadacrysts. Oriented metal inclusions in smelted domains.
NWA 11202	($Fa_{15.0}$), Opx, Aug	Weak, fracture assoc., sulfide dominated, minimal graph assoc	40% in transgressive veins, 50% as large irregular blocks on grain boundaries, 10% coarsely crystalline graphite	Mild: undulose olivine	Weak	No	Lowest smelting extent seen. Plenty of sulfide in fine fractures. Not much metal (but plenty of weathering). Plenty of grain boundary graphite with unusually coarse diamonds. Small chrome spinel inclusions in silicates.
NWA 11893	Ol ($Fa_{16.0}$), Pig	Moderate. Graphite and vein associated sulfide + metal. Some assoc wt transgressive fractures. Trace pore-associated smelting	Crystalline graphite, 30% in transgressive settings, 70% on grain boundaries	Mild: undulose extinction. Networked pyroxenes have low shock.	Moderate	No	Metal+sulfide commonly conjoined, suggests smelting above the eutectic. Plenty of poikiloblastic Pig with olivine chadacrysts – looks like melt network (20% of sample is networked pyroxene). Metal in grain boundary veins.
NWA 5996	90% Ol (Fa_{18}), Pig	Present, obscured by annealing	100% isolated carbon gains amongst fine-grained annealed silicates	Sub-grains after annealing are unshocked	N/A	90% annealed	Fine-grained porous ureilite. The outlines of large, pre-annealing silicate grains are clearly visible. 100% of Ol is annealed, sparsely preserved coarse pyroxene grains is highly porous & contains silicate melt patches
NWA 3156	Ol ($Fa_{18.4-18.6}$), Pig	Intense sulfidation	100% in highly irregular network vein patches	Weak	Weak to absent	No	Extensive sulfidation of all olivine grains. Sulfide inclusions in graphite. Minor silicate melt veins. Graphite occurs in network patches of varying C abundance. Sulfide abundance is very different to Met Bull description.

NWA 5884	Ol ($Fa_{20.2}$), Pig	Moderate, sulfide dominated	95% coarse folded crystalline graphite on grain boundaries, 5% transgressive graphite	Mild, undulose extinction, a few shock twinned grains	Absent	No	Good smelting of Ol only. Silicate melt in grain boundary veins, and in veinlets transecting silicates.
Watson 018	Ol ($Fa_{20.4}$), Pig, Opx	Strong, also affecting pyroxene, vein-associated. Low sulfide	30% in transgressive discontinuous veins, 70% as large irregular blocks on grain boundaries	Strong shock twinning	Strong	Subtle in some grains	Mineral elongation, cross-cut by interconnected D-G veins. Shock twinning roughly parallel to D-G veins, perpendicular to mineral elongation, but smelting cross-cuts shock twinning as well. Both Ol and Px smelted.
NWA 12806	Ol ($Fa_{20.9}$), Pig	Strong. Plumose texture widespread, assoc with metal veins, D-G veins & spots of pore clusters. Variable sulfide	90% in oriented patchy vein-networks	Weak: subtle undulose extinction	Moderate	No	Fresh sample. Sulfide/metal ratio variable in smelted domains; sometimes sulfide more abundant, sometimes less. Plenty of grain boundary metal veins with marginal smelting (variably plumose).
NWA 7630	Ol ($Fa_{21.2}$), Pig	Weak, porosity associated, minor sulfide	70% irregular network patches, 30% in crystalline blocks	None	Absent	None	Sulfide in smelting. Silicate melt along grain boundaries containing spherical metal-sulfide droplets. Cracks in Ol and Px contain silicate melt.
NWA 11755	Ol ($Fa_{21.3}$), Pig, Opx	Smelted domains highly porous (see comment). Minor sulfide.	60% in veins and irregular patches (poor polish), 40% bocks on grain boundaries.	Primary grains have shock twins, annealed sub-grains are unshocked	Strong, partially obscured by annealing	Very coarse partial annealing	All pyroxene grains are full of large pores with silicate melt patches, some enveloping pores. Olivine grains are clear of inclusions. Smelting and porosity are strongly correlated, with plumes of porosity + smelting around graphite. There are transecting "veins" of coarse pore spaces (= transected inclusions) amongst smelting.
NWA 11900	Ol ($Fa_{22.2}$), Opx, Aug	Strong. Plenty in transgressive fractures. Minor pore-associated smelting. Sulfides present but extensive rusting.	40% in transgressive veins and vein-networks, 60% in large blocky grains on grain boundaries	Mild: undulose Ol and Px	Mild	No	Lots of interconnected coarse Opx with Ol chadacrysts, indicating extensive melt network - 30%. Aug coronae around a few rounded Opx grains.
NWA 3140	Ol ($Fa_{22.2}$), Pig	Moderate. Sulfide rich	30% in transgressive vein-networks, 70% as large irregular blocks on triple junctions	Mosaicism	Weak	Weak	Weak Px annealing associated with grain-cutting D-G veins. Obvious fracture-associated smelting.
NWA 2705	Ol ($Fa_{22.3}$), Pig, Opx	Moderate. Low to moderate sulfide	100% in vein-network patches	Strong shock twinning	Strong	Strong coarse partial annealing	Observed sample has no primary pyroxene. Smelted zones are annealed – smelting facilitated annealing. A second stage of unannealed smelting overprints.

NWA 4471	Ol ($Fa_{22.4}$), Pig	Mild, low sulfide, silicate melt in smelted areas	90% in blocky chunks on grain boundaries, 10% transgressive	High, mosaicism, some shock twinning	Moderate	No	Numerous silicate melt patches in many smelted domains (contain metal droplets), associated with grain boundaries. Well-rounded voids imply gas bubbles amongst silicate melt.
NWA 5391	Ol ($Fa_{23.8}$), Pig	Mild, moderately sulfide rich	100% abundant coarse graphite crystals on grain boundaries	Moderate mosaicism, sparse shock twinning	Moderate	No	Plenty of grain boundary silicate melt enveloping graphite and metal/sulfide, some transecting grains. Some graphite inclusions in silicates. Nanoscale sulfide(?) dusting around intragrain silicate melt patches.

*Compositions as reported in the Meteoritical Society Bulletin.

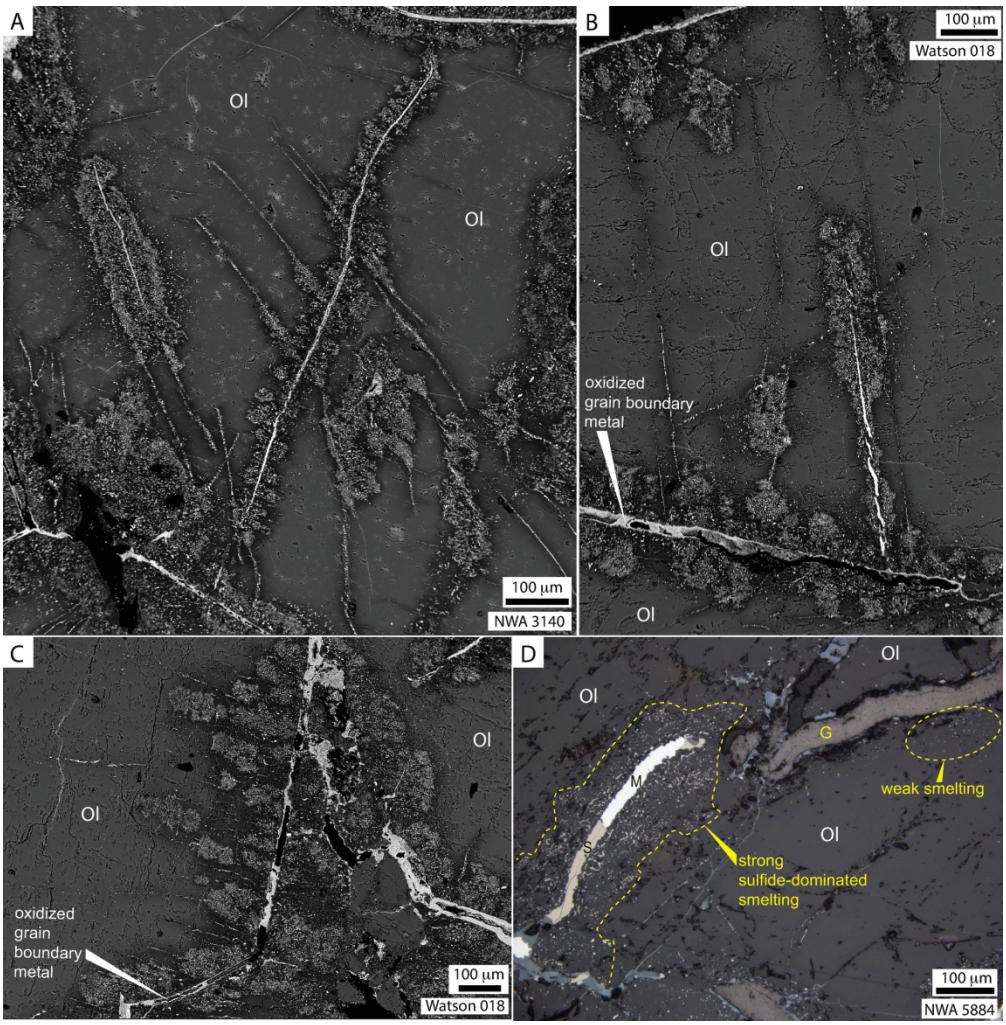

Figure 1. Non-graphite-related smelting characteristics common to most ureilites. (A-C, BSE images) These images highlight fracture-associated smelting and the typical hierarchy of greater smelting around more dominant fractures. Note also the delicate plumose smelting textures in all three images. The darker zones in olivine indicate areas of Fe depletion. (D, reflected light) A clear difference in the intensity of smelting around a metal-troilite vein (M, metal; S, sulfide) compared to a crystalline graphite grain (G). In this case, the smelting is sulfide-dominated, but this is not always so in this textural setting.

172x175mm (300 x 300 DPI)

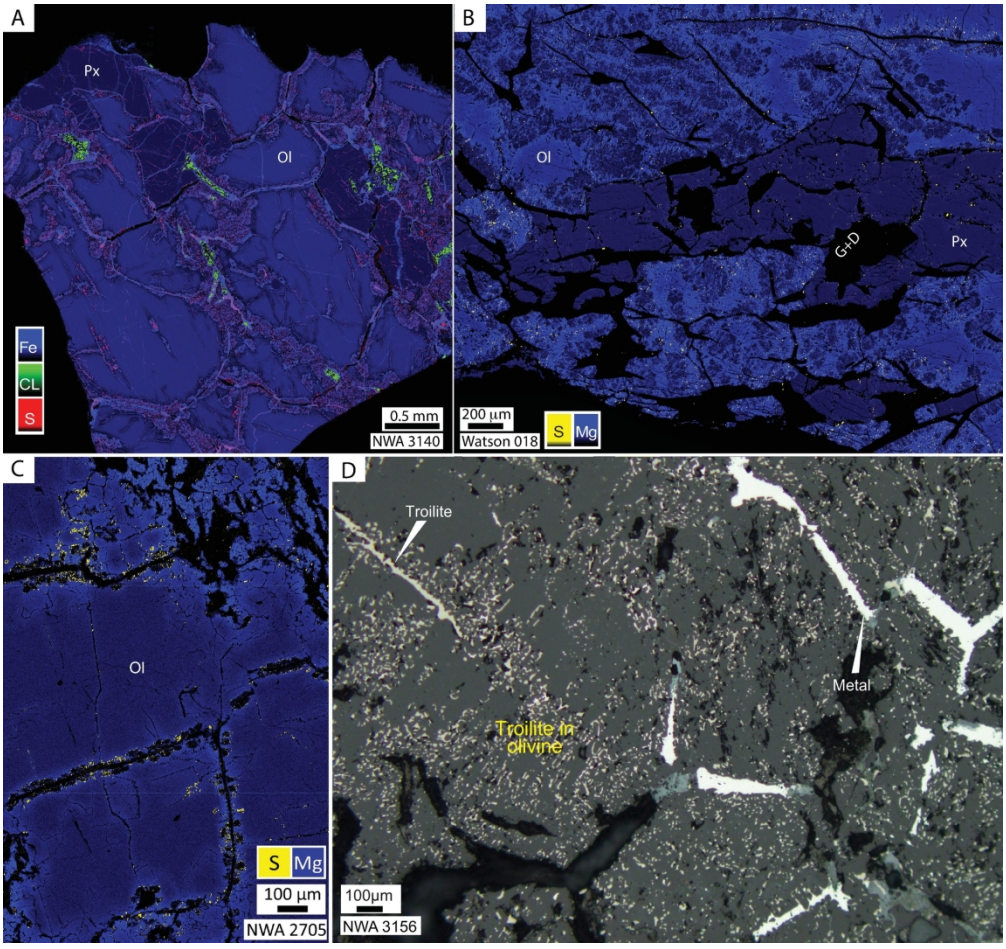

Figure 2. The distribution sulfur in smelted regions in ureilites. (A) A Fe-S-CL map (diamonds in green) highlighting the abundant distribution of fine-grained sulfides in red in all smelted domains (Fe-depleted areas). (B, C) Mg-S maps highlighting abundant sulfide addition associated with smelting. Compare C with Figures 3B and 5. (D, reflected light) Intense sulfidation and associated porosity in NWA 3156.

180x169mm (300 x 300 DPI)

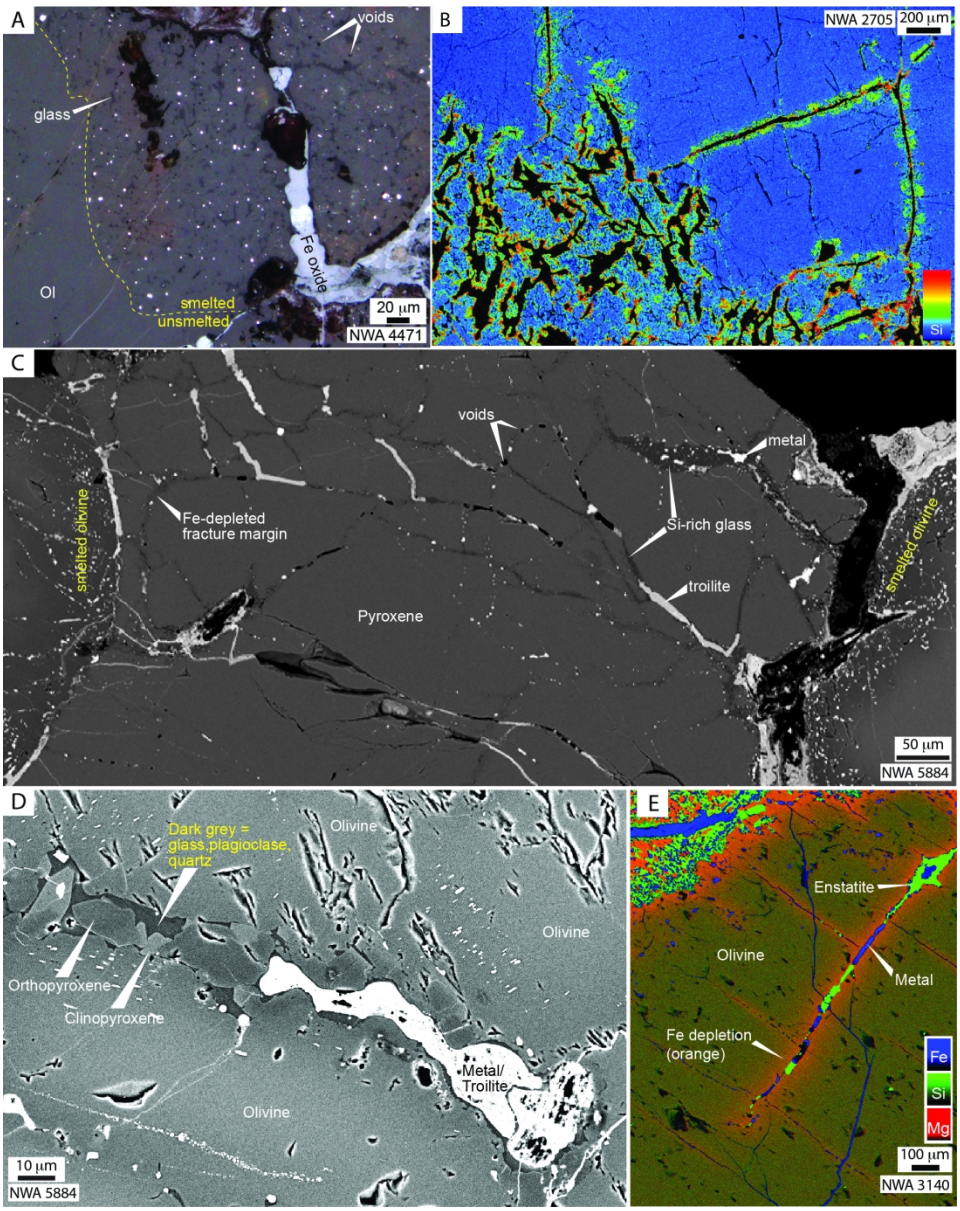

Figure 3. Silicate melt textures. In (A) an association between olivine and pyroxene smelting and silicate melt formation can be seen, with widely dispersed silicate melt pockets developed within the smelted domain. Metal particles are commonly found in the silicate melt pockets. (B) Si map highlighting the production of high silica minerals/melt during smelting; compare with Figures 2C and 6. (C) Silicate melt filled microfractures cutting pyroxene with narrow Fe-depleted domains at the margins. Metal-troilite melt droplets and veins are typically found within the silicate melt. (D) An example of the textures resulting from crystallisation of primary grain-boundary silicate melt, with glass + euhedral pyroxene crystals and encapsulated globular metal/troilite. (E) A Fe-Si-Mg map highlighting enstatite production associated with olivine smelting, and the subtle smelting around small fractures compared that around large.

172x217mm (300 x 300 DPI)

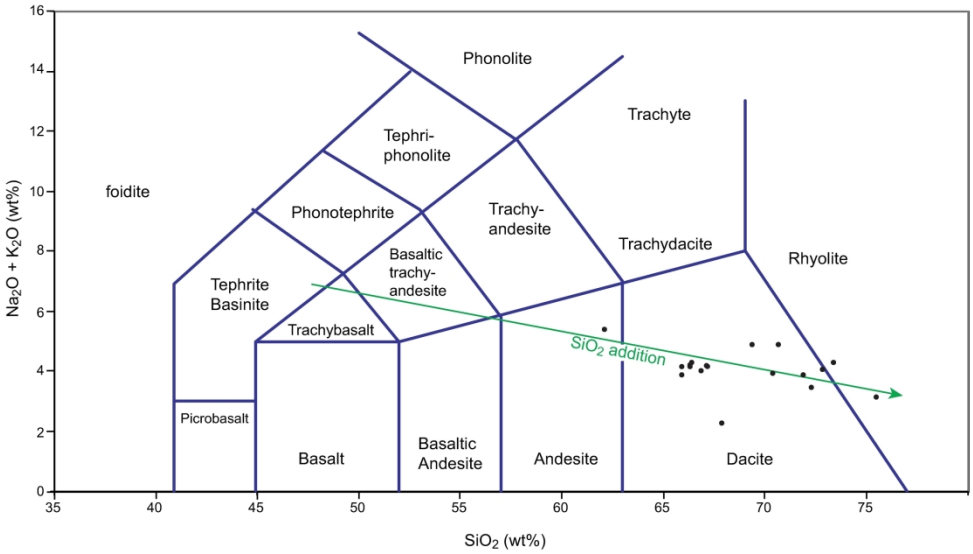

Figure 4. Variation in silicate glass compositions in NWA 4471 compared with a vector for SiO2 addition.

255x155mm (300 x 300 DPI)

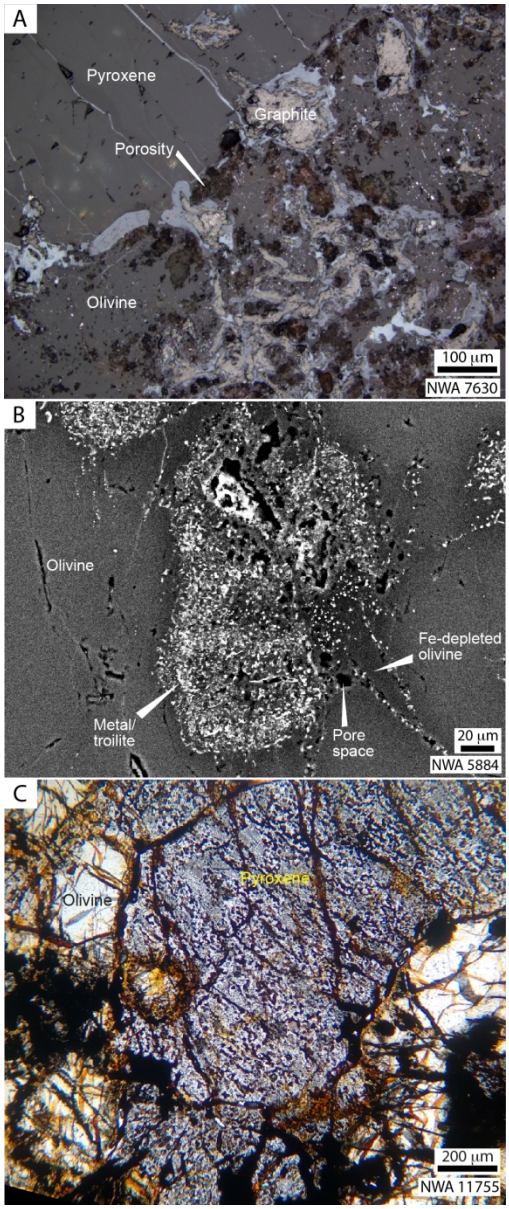

Figure 5. Examples of smelting-associated porosity in ureilites. Some ureilites have extensively developed porosity closely tied to smelted domains such as that shown in (A, reflected light), whereas others have considerably less (compare with Fig. 2D, 3A). (B, BSE) example of the close association between smelted olivine domain and micro-scale porosity. (C, transmitted light) All pyroxenes in NWA 11755 are riddled with inclusions, as shown here, with most consisting of a large void, and some containing sulfides. The olivine in this sample lacks these inclusions, but is very coarsely annealed, which in turn is overprinted by the same intense porosity as shown in (A).

86x205mm (300 x 300 DPI)

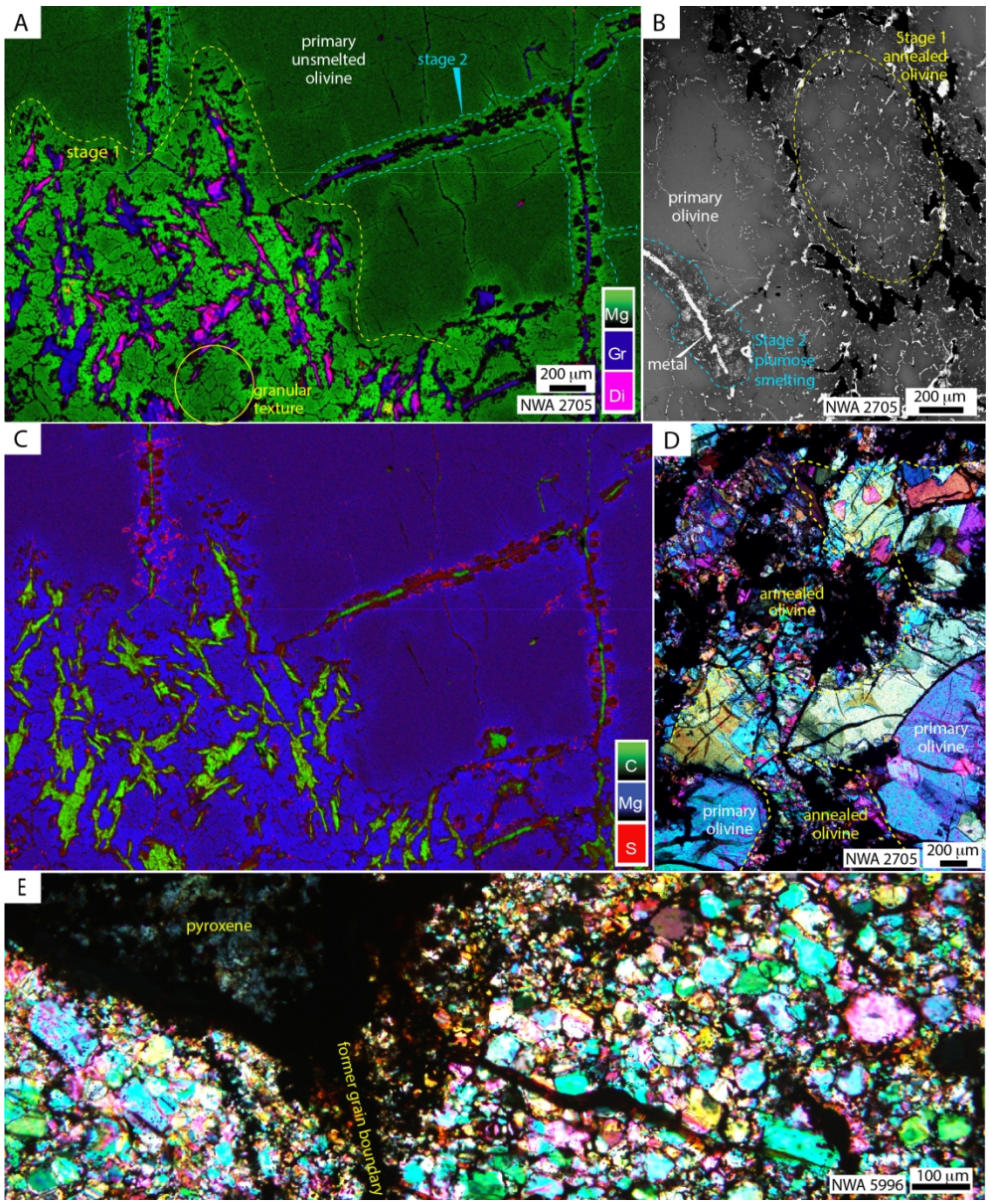

Figure 6. Different views of the two stages of smelting identified in NWA 2705. Stage 1 smelting has an annealed granular texture amongst clusters of distinctive elongate diamond/lonsdaleite (a CL-bright carbon phase) in graphite (A), with metal decorating the margins of the annealed grains (B). Delicate plumose sulfide-rich smelting (B and C) characterizes the second stage of smelting, focused mainly on fractures cutting olivine. (D, cross polarized light) Olivine sub-grains generated by the smelting-associated annealing are over 200 mm across in some cases. (E, cross polarized light) An example of annealed olivine (the numerous colourful sub-grains) from a pervasively annealed fine grained ureilite, NWA 5996.

166x201mm (300 x 300 DPI)

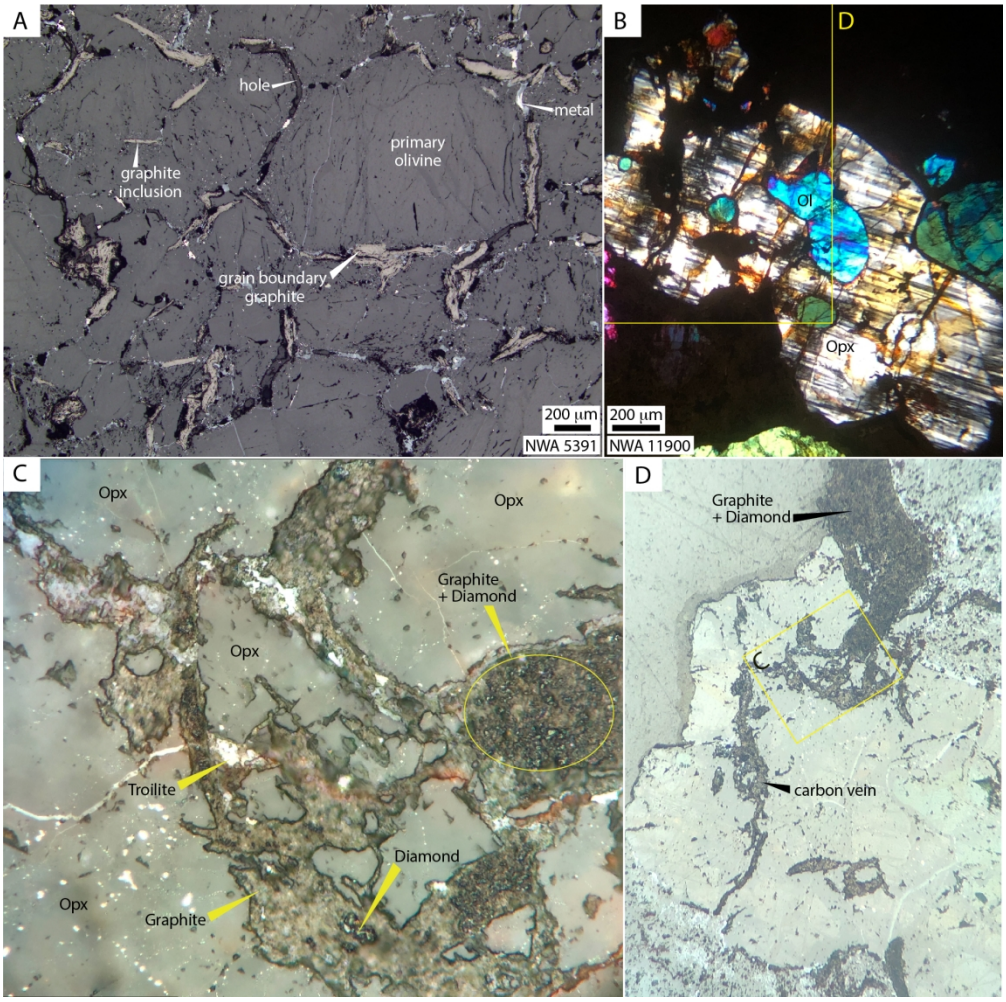

Figure 7. Comparison of syn-peak metamorphic graphite with graphite + diamond in semi-continuous veins cutting across poikiloblastic pyroxene. (A, reflected light) A diamond-free ureilite with minimal smelting, preserving the primary peak metamorphic association of crystalline graphite at the grain boundaries of olivine and pyroxene. Metal veins and holes formed by rusting of metal veins are also seen along grain boundaries.¬ (B-C) An example of a transgressive carbon vein in an augite-bearing ureilite. (B, cross polarized light) shows a large primary poikilitic orthopyroxene grain (Opx) with olivine chadacrysts (Ol), with the area of (D) highlighted. (D, reflected light) shows a narrow vein of carbon entirely transgressing the orthopyroxene grain. (C) shows detail of graphite and diamond within the carbon vein, and the highly irregular nature of the vein margins, indicating a high degree of disequilibrium.

167x166mm (300 x 300 DPI)

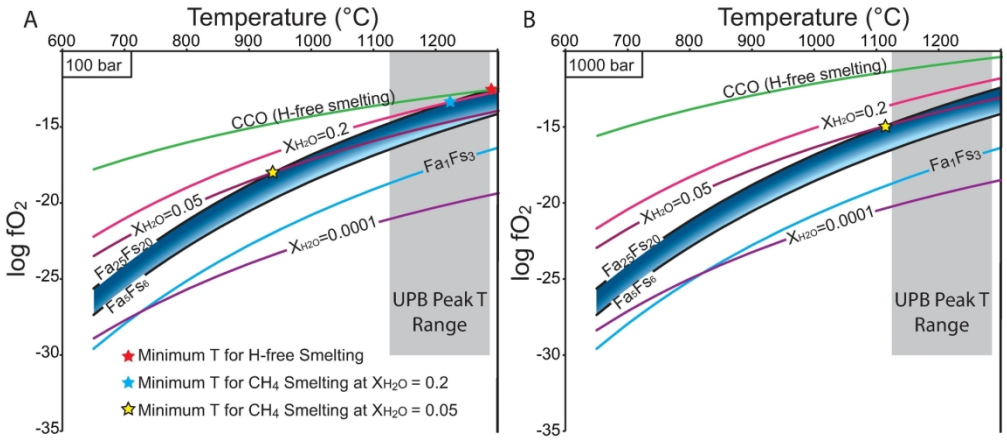

Figure 8. Redox buffer curves relevant to smelting of ureilite olivine and pyroxene compositions at 100 bar (A) and 1000 bar (B) confining pressure. FaxFsx numbers indicate the position of Ol-Px-Fe (OPI) oxygen buffer as a function of the proportions of fayalite in olivine and ferrosilite in orthopyroxene. The blue shaded region indicates the position of the OPI buffer for the natural range of pre-smelted olivine and orthopyroxene compositions in ureilites. The light blue line represents the composition of olivine and orthopyroxene observed in smelted regions: this line represents the oxidation state reached by the smelting reaction. Curves labelled XH2O indicate the position of methane-driven smelting for a CH4-H2O fluid, indicating systems with nearly pure methane, 5% H2O and 20% H2O. It should be noted that H2S has not been considered for this fluid. The CCO buffer (green line) has been plotted to show smelting without H, allowing a comparison with the oxidation state reached by graphite-driven smelting.

169x73mm (300 x 300 DPI)

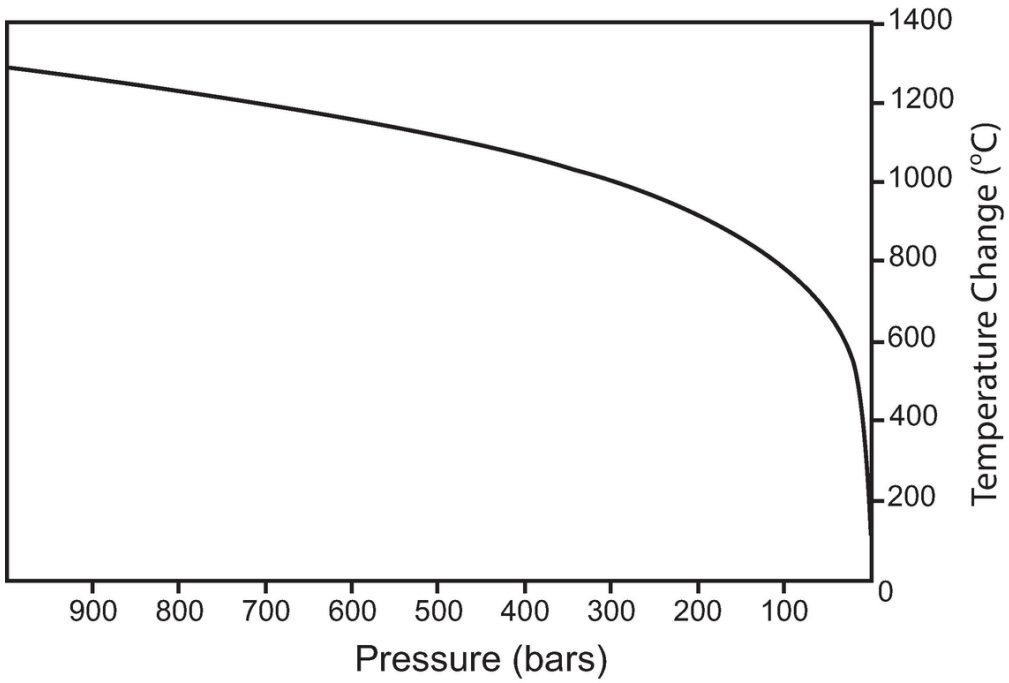

Figure 9. Change in temperature of gas co-existing with silicate melt as a function of pressure decrease.

95x65mm (300 x 300 DPI)

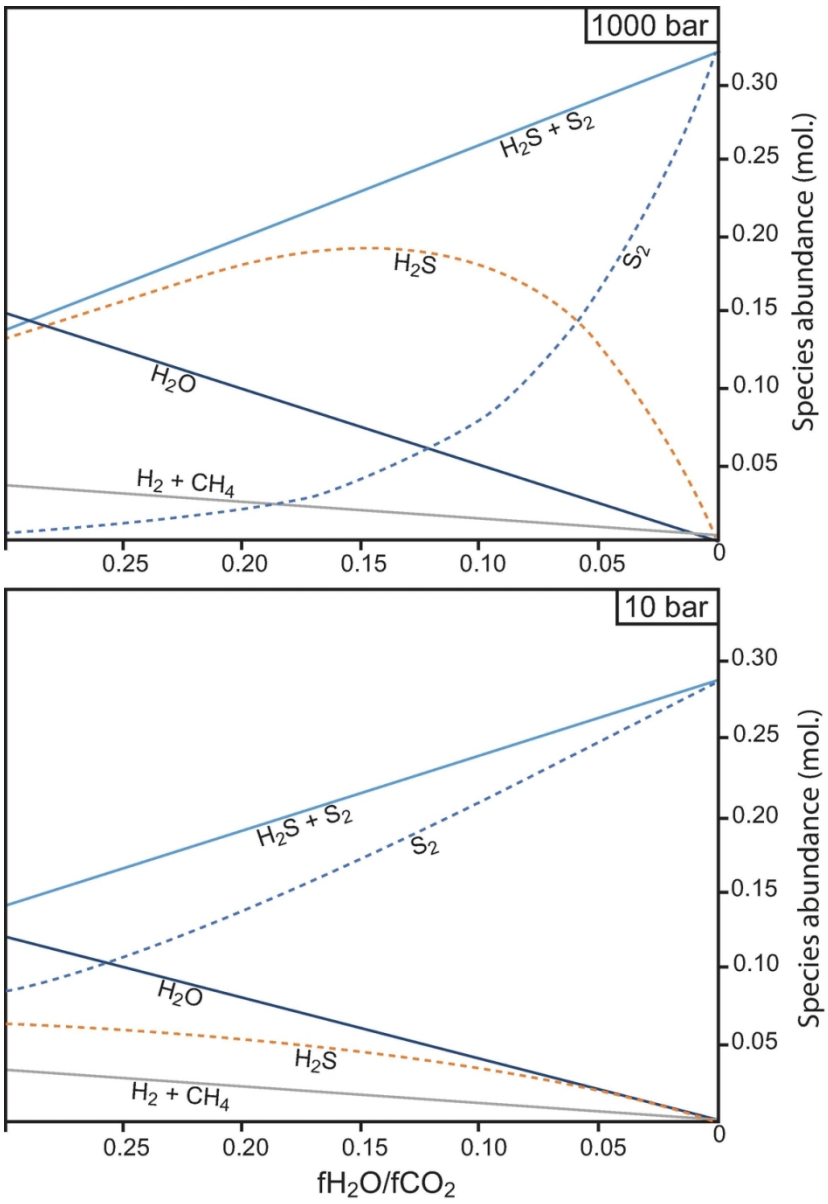

Figure 10. Variations in the proportions of gases coexisting with basaltic silicate melt as a function of the relative pressures of H2O and CO2.

96x140mm (300 x 300 DPI)